International Journal of Heat and Mass Transfer 128 (2019) 999–1016

Contents lists available at ScienceDirect

International Journal of Heat and Mass Transfer

journal homepage: www.elsevier.com/locate/ijhmt

Cascaded lattice Boltzmann method based on central moments for axisymmetric thermal flows including swirling effects

Farzaneh Hajabdollahi *, Kannan N. Premnath, Samuel W.J. Welch

Department of Mechanical Engineering, University of Colorado Denver, 1200 Larimer Street, CO 80217, USA

ARTICLE INFO

Article history:
Received 26 June 2018
Received in revised form 13 September 2018
Accepted 13 September 2018
Available online 21 September 2018

Keywords:
Lattice Boltzmann method
Central moments
Multiple relaxation times
Axisymmetric flows
Thermal convection

ABSTRACT

A cascaded lattice Boltzmann (LB) approach based on central moments and multiple relaxation times to simulate thermal convective flows, which are driven by buoyancy forces and/or swirling effects, in the cylindrical coordinate system with axial symmetry is presented. In this regard, the dynamics of the axial and radial momentum components along with the pressure are represented by means of the 2D Navier-Stokes equations with geometric mass and momentum source terms in the pseudo Cartesian form, while the evolutions of the azimuthal momentum and the temperature field are each modeled by an advection-diffusion type equation with appropriate local source terms. Based on these, cascaded LB schemes involving three distribution functions are formulated to solve for the fluid motion in the meridian plane using a D2Q9 lattice, and to solve for the azimuthal momentum and the temperature field each using a D2Q5 lattice. The geometric mass and momentum source terms for the flow fields and the energy source term for the temperature field are included using a new symmetric operator splitting technique, via pre-collision and post-collision source steps around the cascaded collision step for each distribution function. These result in a particularly simple and compact formulation to directly represent the effect of various geometric source terms consistently in terms of changes in the appropriate zeroth and first order moments. Simulations of several complex buoyancy-driven thermal flows and including rotational effects in cylindrical geometries using the new axisymmetric cascaded LB schemes show good agreement with prior benchmark results for the structures of the velocity and thermal fields as well as the heat transfer rates given in terms of the Nusselt numbers. Furthermore, the method is shown to be second order accurate and significant improvements in numerical stability with the use of the cascaded LB formulation when compared to other collision models for axisymmetric flow simulations are demonstrated.

1. Introduction

Fluid motion in cylindrical coordinates with axial symmetry that is driven by rotational effects and/or thermal buoyancy effects arise widely in a number of engineering applications and geophysical contexts (e.g., [1–5]). Some examples of technological applications encountering heat and mass transfer effects in axisymmetric flows include pipeline systems, heat exchangers, solar energy conversion devices, crystal growth and material processing systems, electronic cooling equipment and turbomachinery. Computational methods play an important role for both fundamental studies of the fluid mechanics and heat transfer aspects and as predictive tools for engineering design of such systems. In general, fluid motion in cylindrical coordinates due to swirling effects and buoyancy forces, and accompanied by thermal and mass transport is three-dimensional (3D) in nature. Computational effort for such problems can be significantly reduced if axial symmetry, which arise in various contexts, can be exploited; in such cases the system of equations can be reduced to a set of quasi-two-dimensional (2D) problems in the meridian plane, where the simulations can be performed for broader ranges of the parameter spaces more efficiently. Traditionally, numerical schemes based on finite difference, finite volume or finite elements were constructed to solve the axisymmetric Navier-Stokes (NS) equations for the fluid flow along with the advection-diffusion equation for the energy transport (e.g., [6,7]).

On the other hand, lattice Boltzmann (LB) methods, which arise as minimal kinetic models of the Boltzmann equation, has attracted much attention and application to a wide range of fluid flows and heat and mass transfer problems [8–12]. They can be characterized as mesoscopic computational approaches, which

* Corresponding author.
E-mail addresses: farzaneh.hajabdollahiouderji@ucdenver.edu (F. Hajabdollahi), kannan.premnath@ucdenver.edu (K.N. Premnath), Sam.Welch@ucdenver.edu (S.W.J. Welch).

https://doi.org/10.1016/j.ijheatmasstransfer.2018.09.059
0017-9310/

have the following unique features and advantages: Its streaming step is linear and exact and all nonlinearity is modeled locally in the collision step; by contrast, the convective term in the NS equation is nonlinear and nonlocal. As a result, the pressure field is obtained locally in the LB methods, circumventing the need for the solution of the time consuming elliptic Poisson equation as in traditional methods. The exact-advection in the streaming step combined with the collision step based on a relaxation model leads to a second order accurate method with relatively low numerical dissipation. The kinetic model for the collision step can be tailored to introduce additional physics as necessary and its additional degree of freedom can be tuned to improve numerical stability. Various boundary conditions for complex geometries can be represented using relatively simple rules for the particle populations. Finally, the locality of the method makes it amenable for almost ideal implementation on parallel computers for large scale flow simulations.

Following an approach for the solution of the Boltzmann equation in cylindrical coordinates [13], during the last two decades, various LB schemes for athermal flows (i.e., without heat transfer effects) have been introduced [14–22]. These approaches can be categorized according to the following: (i) Coordinate transformation method [14–18], in which the axisymmetric mass and momentum equations are reformulated as quasi-2D flow equations in the Cartesian forms with additional geometric source terms and then solved using a LB scheme. (ii) Vorticity-stream function approach [19], where LB models are introduced to simulate flows in the cylindrical coordinates written in terms of the vorticity and stream function equations. (iii) Radius-weighted formulation [20], in which a simplified LB method is derived from a discretization of the continuous Boltzmann equation in cylindrical coordinates recast in a radius-weighted form. An analysis of these axisymmetric LB models were performed by [21]. Generally, these approaches use a popular single relaxation time (SRT) model for the representation of the collision step in the LB scheme.

Further progress in the LB methods for the simulation of axisymmetric thermal flows have been reported in various studies [23–32]. Earlier LB models in this regard [23,24] used an hybrid approach, in which the energy equation was solved via a finite difference scheme. Later, [25,26] solved the axisymmetric equation for the temperature field written in terms of a pseudo-2D advection-diffusion equation with a source term using a LB scheme based on a separation distribution function from that for the flow field. On the other hand, [27,28] extended the radius-weighted formulation approach for axisymmetric fluid flow [20] for the simulation of thermal energy transport. A fractional-step based LB flux solver for axisymmetric thermal flow was presented in [30]. All these approaches were based on the common SRT model [33], in which, during the collision step, the distribution functions relax to their local equilibria using a single relaxation parameter. This was further extended by the introduction of two tunable parameters as coefficients to the additional gradient terms in the equilibrium distribution functions [32]. Generally, SRT based LB schemes are known to be susceptible to numerical instabilities for convection-dominated flows or fluids with relatively low values of transport coefficients. In order to address this issue, the collision step based on a multiple relaxation time (MRT) model [34] has been constructed, in which raw moments of different orders relax at different rates. Few MRT LB schemes for axisymmetric thermal convective flows have recently been developed [26,29,30].

On the other hand, further improvements to the collision step enhancing the flow and thermal transport modeling capabilities can be achieved via the introduction of the cascaded collision model [35]. In this approach, the effects of collisions are represented in terms of relaxation of different orders of central moments, which are obtained by shifting the particle velocity, by the local fluid velocity at different rates. As the collision model is prescribed based on a local moving frame of reference, the relaxation steps for successive higher order moments exhibit a cascaded structure. The cascaded collision formulation was shown to be equivalent to considering relaxation to a generalized equilibrium in the rest or lattice frame of reference [36], and was augmented with forcing terms in 2D and 3D in [37,38]. Improvements in the numerical properties achieved using such advanced cascaded collision models based on central moments were recently demonstrated [39,40]. A modified formulation based on central moments involving relaxation to discrete equilibria rather than continuous Maxwellian equilibria was also proposed [41]. In order to accelerate convergence of steady flows, a preconditioned cascaded LB method was constructed and studied in [42], and whose Galilean invariance properties were significantly improved via corrections to equilibria in [43]. The cascaded LB scheme has recently been extended for simulating flows with heat transfer in 2D [44,45] and in 3D in our recent work [46]. Some related recent papers that discuss about the forcing schemes as well as thermal sources are [47–50]. However, for axisymmetric thermal convective flows including rotational effects, no such advanced LB schemes are available in the literature.

In this work, we present a new cascaded LB formulation for thermal flows in cylindrical coordinates with axial symmetry, and including rotational effects. The mass, momentum (i.e., for the axial, radial and azimuthal components) and energy equations rewritten in pseudo-2D Cartesian forms in the meridian plane contain additional geometric source terms, which are included in the respective cascaded LB schemes via a novel symmetric time-split formulation that we developed recently [50]. In this approach, three separate distribution functions are considered: one for the density, axial and radial momentum components, the second for the azimuthal momentum component and, finally, the third for the temperature field. Each of the three distribution functions evolves according to a cascaded LB scheme. For this triple distribution functions framework, a two-dimensional, nine velocity (D2Q9) model is used to solve for the axisymmetric NS equations for the axial and radial momentum components, while a two-dimensional five velocity (D2Q5) model is employed to compute the azimuthal momentum and the temperature field, both of whose evolution are represented by advection-diffusion equations with source terms. The use of symmetric operator split formulations based on pre-collision and post-collision source steps with a half time step in each case for incorporating the geometric source terms for axisymmetric thermal flows including swirl effects leads to a particulary simplified formulation. Such an approach is consistent with the classical Strang splitting. As will be shown later in this paper, the application of central moments based cascaded LB schemes using MRT can significantly enhance the numerical stability of axisymmetric LB simulations allowing broader range of parameter spaces more efficiently, and the use of symmetric operator splitting yields a scheme that is second order accurate [50]. Such an axisymmetric cascaded LB formulation for the simulation of thermally stratified and/or rotating flows in cylindrical geometries can lead to reduced computational and memory costs when compared to a 3D cascaded LB scheme. Several numerical axisymmetric benchmark problems focusing on buoyancy-driven flows and rotational effects are considered to validate our operator-split axisymmetric cascaded LB schemes for thermal flows. These include the Taylor-Couette flow, natural convection in an annulus between two co-axial vertical cylinders, Rayleigh-Benard convection in a vertical cylinder, cylindrical lid-driven cavity flow, mixed convection in a tall vertical annulus and melt flow during Czochralski crystal growth in a vertical rotating cylinder.

This paper is organized as follows. In the next section (Section 2), cascaded LB methods for axisymmetric thermal flows

with swirl effects using a symmetric operator split formulation for the various geometric sources and forces are presented. Numerical results for various benchmark problems are presented and discussed in Section 3. Finally, the paper concludes with a summary in Section 4.

2. Cascaded LB methods for axisymmetric thermal convective flows with swirling effects: symmetric operator splitting formulation

We will now present cascaded LB methods based on central moments and MRT for the computation of thermal convective flows in the cylindrical coordinates with axial symmetry, by also taking into account azimuthal rotational/swirling effects. A triple distribution functions based LB approach is considered, where the geometric source terms arising in the pseudo-2D macroscopic equations are represented using symmetric operator splitting around the cascaded collision steps [50]. The solution of the resulting cascaded LB models then yields the local fluid flow variables such as the radial, axial and azimuthal velocity fields, pressure (or density) field, and the temperature field in the meridian plane. First, we summarize the macroscopic governing equations for axisymmetric thermal flows subjected to rotation/swirl.

2.1. Governing equations for thermal flows in cylindrical coordinates with axial symmetry

For incompressible, axisymmetric thermal flows subjected to rotational/swirling effects, the macroscopic governing equations in the cylindrical coordinate system (r,θ,z) can be written as (e.g., [20,27])

$$\partial_t\rho+\partial_r(\rho u_r)+\partial_z(\rho u_z)=-\rho\frac{u_r}{r}, \tag{1a}$$

$$\begin{aligned}&\partial_t(\rho u_r)+\partial_r\left(\rho u_r^2\right)+\partial_z(\rho u_r u_z)\\&\quad=-\partial_r p+\partial_r(2\mu\partial_r u_r)+\partial_z[\mu(\partial_z u_r+\partial_r u_z)]\\&\qquad+\rho\frac{u_\theta^2}{r}-\rho\frac{u_r^2}{r}+2\mu\frac{\partial_r u_r}{r}-2\mu\frac{u_r}{r^2}+F_r^b,\end{aligned} \tag{1b}$$

$$\begin{aligned}&\partial_t(\rho u_z)+\partial_r(\rho u_r u_z)+\partial_z\left(\rho u_z^2\right)\\&\quad=-\partial_z p+\partial_r[\mu(\partial_r u_z+\partial_z u_r)]+\partial_z(2\mu\partial_z u_z)-\rho\frac{u_r u_z}{r}\\&\qquad+\mu\frac{(\partial_z u_r+\partial_r u_z)}{r}+F_z^b,\end{aligned} \tag{1c}$$

$$\begin{aligned}&\partial_t(\rho u_\theta)+\partial_r(\rho u_r u_\theta)+\partial_z(\rho u_z u_\theta)\\&\quad=\nu\left[\frac{\partial^2}{\partial r^2}(\rho u_\theta)+\frac{\partial^2}{\partial z^2}(\rho u_\theta)\right]-2\rho\frac{u_r u_\theta}{r}+\rho\frac{\nu}{r}\partial_r u_\theta-\rho\frac{\nu u_\theta}{r^2},\end{aligned} \tag{1d}$$

$$\partial_t\phi+\partial_r(u_r\phi)+\partial_z(u_z\phi)=\partial_r\left(D_\phi\partial_r\phi\right)+\partial_z\left(D_\phi\partial_z\phi\right)-\frac{u_r\phi}{r}+\frac{D_\phi}{r}\partial_r\phi. \tag{1e}$$

Here, r,z and θ represent the coordinates in the radial, axial and azimuthal directions, respectively; accordingly, u_r,u_z and u_θ denote the fluid velocity components in the respective directions, and F_r^b and F_z^b are radial and axial components of the external body forces, respectively. ρ and p represent the density and pressure, respectively, while ν and $\mu=\rho\nu$ correspond to the kinematic and dynamic viscosities of the fluid, respectively. ϕ is the passive scalar variable, which is the temperature field T in the present study (i.e., $\phi=T$) and D_ϕ is the coefficient of diffusivity. Eqs. (1a)–(1c) represent the axisymmetric NS equations for the axial and radial components of the velocity field in the meridian plane. The structure of the evolution equations for the azimuthal momentum (ρu_θ) and the scalar field (ϕ) given in Eqs. (1d) and (1e) respectively, is similar in form, viz., an advection-diffusion equation with a source, and hence they can be solved using the same numerical procedures.

In order to represent the above macroscopic equations in cylindrical coordinates in a set of pseudo-2D Cartesian forms, we apply the following coordinate/variable transformations:

$$(r,z)\mapsto(y,x),\quad (u_r,u_z)\mapsto(u_y,u_x),\quad \rho u_\theta\mapsto\psi. \tag{2}$$

Then, the resulting equations in pseudo-Cartesian forms involve additional terms when compared to the standard flow and thermal transport equations in 2D, which can be regarded as geometric source terms. The latter will be introduced via a symmetric operator splitting technique in the respective cascaded LB formulation in the following. Thus, the mass and momentum equations for the fluid motion in the meridian plane (Eqs. (1a)–(1c)) can be written in pseudo-2D Cartesian forms as

$$\partial_t\rho+\partial_y(\rho u_y)+\partial_x(\rho u_x)=M^A, \tag{3a}$$

$$\begin{aligned}&\partial_t(\rho u_x)+\partial_r\left(\rho u_x^2\right)+\partial_y(\rho u_x u_y)\\&\quad=-\partial_x p+\partial_x[2\mu\partial_x u_x]+\partial_y\left[\mu\left(\partial_y u_x+\partial_x u_y\right)\right]+F_x^A+F_x^b,\end{aligned} \tag{3b}$$

$$\begin{aligned}&\partial_t(\rho u_y)+\partial_x(\rho u_x u_y)+\partial_y\left(\rho u_y^2\right)\\&\quad=-\partial_y p+\partial_x\left[\mu\left(\partial_x u_y+\partial_y u_x\right)\right]+\partial_y\left[2\mu\partial_y u_y\right]+F_y^A+F_y^b,\end{aligned} \tag{3c}$$

where the geometric mass source M^A and the geometric momentum source vector $\boldsymbol{F}^A=\left(F_x^A,F_y^A\right)$ can be represented as

$$M^A=-\rho\frac{u_y}{y}, \tag{4a}$$

$$F_x^A=-\rho\frac{u_x u_y}{y}+\mu\frac{\left(\partial_x u_y+\partial_y u_x\right)}{y}, \tag{4b}$$

$$F_y^A=\frac{\psi^2}{\rho y}-\rho\frac{u_y^2}{y}+2\mu\frac{\partial_y u_y}{y}-2\mu\frac{u_y}{y^2}. \tag{4c}$$

Then, the total force $\boldsymbol{F}=(F_x,F_y)$ in this formulation becomes

$$F_x=F_x^A+F_x^b,\quad F_y=F_y^A+F_y^b. \tag{5}$$

Here, the body force $\boldsymbol{F}^b=\left(F_x^b,F_y^b\right)$ could be a volumetric force such as the buoyancy force or the Lorentz force. Similarly, the azimuthal momentum equation for $\psi=\rho u_\theta$ can be written as

$$\partial_t\psi+\partial_x(u_x\psi)+\partial_y(u_y\psi)=D_\psi\left(\partial_x^2\psi+\partial_y^2\psi\right)+S_\psi, \tag{6}$$

where the corresponding geometric source term S_ψ can be expressed as

$$S_\psi=-\frac{2u_y\psi}{y}+\frac{\mu}{y}\partial_y\left(\frac{\psi}{\rho}\right)-\frac{\nu\psi}{y^2}, \tag{7}$$

and D_ψ is the coefficient of diffusivity, which is equal to the kinematic viscosity of the fluid ν, i.e. $D_\psi=\nu$. Finally, the axisymmetric advection-diffusion equation for the scalar, i.e., the temperature field $(\phi=T)$ in the pseudo-2D cartesian coordinate system reads as

$$\partial_t\phi+\partial_x(u_x\phi)+\partial_y(u_y\phi)=\partial_x\left(D_\phi\partial_x\phi\right)+\partial_y\left(D_\phi\partial_y\phi\right)+S_\phi, \tag{8}$$

where the source term S_ϕ is given as

$$S_\phi=-\frac{u_y\phi}{y}+\frac{D_\phi}{y}\partial_y\phi. \tag{9}$$

Our goal, then, is to represent the evolution of the axial and radial momentum components along with density or pressure (Eqs. (3)–(5)) using a distribution function f_α, azimuthal

momentum (Eqs. (6) and (7)) using another distribution function g_α, and the scalar temperature field (Eqs. (8) and (9)) using a third distribution function h_α. We use a D2Q9 lattice for f_α, while for both g_α and h_α, a D2Q5 lattice would suffice since to represent advection-diffusion type equations, the lattice is required to satisfy only a lower degree of symmetry than the lattice used for the Navier-Stokes equations. In each case, a cascaded LB scheme based on a symmetric operator splitting will be constructed in the following.

2.2. Cascaded LB scheme for axial and radial velocity fields: operator splitting for mass and momentum source terms

In order to consistently include the geometric mass and momentum sources along with any external body force given in Eqs. (4) and (5) in a cascaded LB scheme, we will employ a symmetric operator splitting strategy with two half force steps around its collision term [50]. First, we define the following components of the particle velocities for the D2Q9 lattice:

$$|e_x\rangle = (0,1,0,-1,0,1,-1,-1,1)^\dagger, \tag{10a}$$

$$|e_y\rangle = (0,0,1,0,-1,1,1,-1,-1)^\dagger, \tag{10b}$$

where † is the transpose operator and their components for any particle direction α are denoted by $e_{\alpha x}$ and $e_{\alpha y}$, where $\alpha = 0, 1, \ldots, 8$. We also need the following 9-dimensional vector

$$|1\rangle = (1,1,1,1,1,1,1,1,1)^\dagger \tag{11}$$

whose inner product with the distribution function f_α defines its zeroth moment. Here, and in the following, we have used the standard Dirac's bra-ket notation to represent the vectors. The corresponding nine orthogonal basis vectors may be represented by (e.g., [37]):

$$\begin{aligned}
&K_0 = |1\rangle, \quad K_1 = |e_x\rangle, \quad K_2 = |e_y\rangle, \quad K_3 = 3\left|e_x^2 + e_y^2\right\rangle - 4|1\rangle,\\
&K_4 = \left|e_x^2 - e_y^2\right\rangle, \quad K_5 = |e_x e_y\rangle, \quad K_6 = -3|e_x^2 e_y\rangle + 2|e_y\rangle,\\
&K_7 = -3\left|e_x e_y^2\right\rangle + 2|e_x\rangle, \quad K_8 = 9\left|e_x^2 e_y^2\right\rangle - 6\left|e_x^2 + e_y^2\right\rangle + 4|1\rangle.
\end{aligned} \tag{12}$$

Here and henceforth, symbols such as $|e_x^2 e_y\rangle = |e_x e_x e_y\rangle$ denote a vector that result from the elementwise vector multiplication of vectors $|e_x\rangle, |e_x\rangle$ and $|e_y\rangle$. The above set of vectors can be organized by the following orthogonal matrix

$$\mathbf{K} = [K_0, K_1, K_2, K_3, K_4, K_5, K_6, K_7, K_8], \tag{13}$$

which maps changes of moments under collisions due to a cascaded central moment relaxation back to changes in the distribution function (see below). As the cascaded collision operator is built on the moment space, we first define the central moments and raw moments of order $(m+n)$ of the distribution function f_α and its equilibrium f_α^{eq} as

$$\begin{pmatrix} \hat{\kappa}_{x^m y^n} \\ \hat{\kappa}^{eq}_{x^m y^n} \end{pmatrix} = \sum_\alpha \begin{pmatrix} f_\alpha \\ f_\alpha^{eq} \end{pmatrix} (e_{\alpha x} - u_x)^m (e_{\alpha y} - u_y)^n, \tag{14}$$

and

$$\begin{pmatrix} \hat{\kappa}'_{x^m y^n} \\ \hat{\kappa}^{eq'}_{x^m y^n} \end{pmatrix} = \sum_\alpha \begin{pmatrix} f_\alpha \\ f_\alpha^{eq} \end{pmatrix} e_{\alpha x}^m e_{\alpha y}^n, \tag{15}$$

respectively. Here, and in what follows, the prime ($'$) symbols denote various raw moments. The central moments of the equilibrium are constructed to be equal to those for the Maxwellian, which then serve as attractors during the cascaded collision represented as a relaxation process [35]. In the following, an operator splitting based cascaded LB scheme will be constructed to solve Eqs. (3)–(5). First, we represent the solution of the mass and momentum equations in the meridian plane (Eq. (3)) without the respective source terms (i.e., $M_A, F_x^A, F_x^b, F_y^A, F_y^b$) by means of the evolution of the distribution function f_α using the usual collision and streaming steps (**C** and **S**, respectively) as

$$\textbf{Step C}: \quad f_\alpha^p = f_\alpha + (\mathbf{K}\cdot\widehat{\mathbf{p}})_\alpha, \tag{16a}$$

$$\textbf{Step S}: \quad f_\alpha(\mathbf{x},t) = f_\alpha^p(\mathbf{x} - \mathbf{e}_\alpha \Delta t, t), \tag{16b}$$

where $\mathbf{e}_\alpha = (\mathbf{e}_{\alpha x}, \mathbf{e}_{\alpha y})$, Δt is the time step, f_α^p is the post-collision distribution function at a location $\mathbf{x}$ and time t. $\widehat{\mathbf{p}} = (\widehat{p}_0, \widehat{p}_1, \widehat{p}_2 \ldots \widehat{p}_8)$ denotes the changes of different moments under collision based on the relaxation of central moments to their equilibria in a cascaded fashion [35]. With the mass and momentum being conserved during collision $\widehat{p}_0 = \widehat{p}_1 = \widehat{p}_2 = 0$, and the changes in the higher order non-conserved moments are given by [35–37]

$$\begin{aligned}
\widehat{p}_3 &= \frac{\omega_3}{12}\left\{2c_s^2\rho + \rho\left(u_x^2 + u_y^2\right) - \left(\widehat{\kappa}'_{xx} + \widehat{\kappa}'_{yy}\right)\right\},\\
\widehat{p}_4 &= \frac{\omega_4}{4}\left\{\rho\left(u_x^2 - u_y^2\right) - \left(\widehat{\kappa}'_{xx} - \widehat{\kappa}'_{yy}\right)\right\},\\
\widehat{p}_5 &= \frac{\omega_5}{4}\left\{\rho u_x u_y - \widehat{\kappa}'_{xy}\right\},\\
\widehat{p}_6 &= \frac{\omega_6}{4}\left\{2\rho u_x^2 u_y + \widehat{\kappa}'_{xxy} - 2u_x\widehat{\kappa}'_{xy} - u_y\widehat{\kappa}'_{xx}\right\} - \frac{1}{2}u_y(3\widehat{p}_3 + \widehat{p}_4) - 2u_x\widehat{p}_5,\\
\widehat{p}_7 &= \frac{\omega_7}{4}\left\{2\rho u_x u_y^2 + \widehat{\kappa}'_{xyy} - 2u_y\widehat{\kappa}'_{xy} - u_x\widehat{\kappa}'_{yy}\right\} - \frac{1}{2}u_x(3\widehat{p}_3 - \widehat{p}_4) - 2u_y\widehat{p}_5,\\
\widehat{p}_8 &= \frac{\omega_8}{4}\left\{c_s^4\rho + 3\rho u_x^2 u_y^2 - \left[\widehat{\kappa}'_{xxyy} - 2u_x\widehat{\kappa}'_{xyy} - 2u_y\widehat{\kappa}'_{xxy} + u_x^2\widehat{\kappa}'_{yy} + u_y^2\widehat{\kappa}'_{xx}\right.\right.\\
&\quad \left.\left. + 4u_x u_y\widehat{\kappa}'_{xy}\right]\right\} - 2\widehat{p}_3 - \frac{1}{2}u_y^2(3\widehat{p}_3 + \widehat{p}_4) - \frac{1}{2}u_x^2(3\widehat{p}_3 - \widehat{p}_4)\\
&\quad - 4u_x u_y\widehat{p}_5 - 2u_y\widehat{p}_6 - 2u_x\widehat{p}_7.
\end{aligned} \tag{17}$$

Here, $\omega_3, \omega_4 \ldots \omega_8$ are relaxation parameters, where ω_3, ω_4 and ω_5 are related to the bulk and shear viscosities and the other ω_i influence the numerical stability of the method. In particular, the bulk viscosity is given by $\xi = c_s^2\left(\frac{1}{\omega_3} - \frac{1}{2}\right)\Delta t$ and the shear viscosity by $\nu = c_s^2\left(\frac{1}{\omega_j} - \frac{1}{2}\right)/\Delta t$, where $j = 4, 5$, and $c_s^2 = c^2/3$, with $c = \Delta x/\Delta t$. In this work, we consider the lattice units, where $\Delta x = \Delta t = 1$ and hence the speed of sound $c_s = 1/\sqrt{3}$, and the higher order relaxation parameters ω_6, ω_7 and ω_8 are set to unity for simplicity. After the streaming step (see Eq. (16b)), the output density field and the velocity field components (designated with a superscript "o") as the zeroth and first moments of f_α, respectively:

$$\rho^o = \sum_{\alpha=0}^{8} f_\alpha, \quad \rho^o u_x^o = \sum_{\alpha=0}^{8} f_\alpha e_{\alpha x}, \quad \rho^o u_y^o = \sum_{\alpha=0}^{8} f_\alpha e_{\alpha y} \tag{18}$$

and $p = c_s^2\rho^o$. We then introduce the influence of the mass source M^A in Eq. (3a) and the momentum sources $F_x^A = F_x^A + F_x^b$ and $F_y = F_y^A + F_y^b$ in Eqs. (3b) and (3c), respectively, as the solution of the following two sub problems, referred to as the mass source step **M** and momentum source step **F**, respectively:

$$\text{Step } \mathbf{M}: \ \partial_t\rho = M^A, \tag{19a}$$

$$\text{Step } \mathbf{F}: \ \partial_t(\rho\mathbf{u}) = \mathbf{F} = \mathbf{F}^A + \mathbf{F}^b, \tag{19b}$$

where $\mathbf{u} = (u_x, u_y)$ and $\mathbf{F}_A = \left(F_x^A, F_y^b\right)$ etc. In our previous work [50], we constructed a symmetric operator splitting based approach to incorporate a single momentum source in a cascaded LB method. In the present work, we further extend this approach to symmetric splitting of multiple operators related to mass and momentum sources. In other words, we perform two symmetric steps of half

time steps of length $\Delta t/2$ of $\mathbf{M}$ and $\mathbf{F}$, one before and the other after the collision step. The overall symmetrized operator splitting based cascaded LB algorithm implementing all the four operators ($\mathbf{C}, \mathbf{S}, \mathbf{M}$ and $\mathbf{F}$) during the time interval $[t, t+\Delta t]$ may be written as

$$f_\alpha(\mathbf{x}, t+\Delta t) = \mathbf{M}^{1/2}\mathbf{F}^{1/2}\mathbf{C}\mathbf{F}^{1/2}\mathbf{M}^{1/2}\mathbf{S}f_\alpha(\mathbf{x}, t), \tag{20}$$

where $\mathbf{M}^{1/2}$ and $\mathbf{F}^{1/2}$ represent solving Eqs. (19a) and (19b), respectively, over time step $\Delta t/2$. Both of these steps introduce the effect of geometric mass and momentum source and the body forces directly into the moment space.

Solving Eqs. (19a) and (19b) for the first part of symmetric sequence needed in Eq. (20) yields $\rho - \rho^o = M^A\frac{\Delta t}{2}$, $\rho u_x - \rho u_x^o = F_x\frac{\Delta t}{2}$ and $\rho u_y - \rho u_y^o = F_y\frac{\Delta t}{2}$. Thus, we have

$$\text{Pre-collision Mass Source Step } \mathbf{M}^{1/2}: \ \rho = \rho^o + M^A\frac{\Delta t}{2}, \tag{21a}$$

$$\text{Pre-collision Momentum Source Step } \mathbf{F}^{1/2}: \ \rho u_x = \rho u_x^o + F_x\frac{\Delta t}{2}, \tag{21b}$$

$$\rho u_y = \rho u_y^o + F_y\frac{\Delta t}{2}, \tag{21c}$$

where M^A, F_x and F_y are given in Eqs. (4a)–(4c) and (5), and ρ^o, u_x^o and u_y^o are obtained using Eq. (18). Based on Eq. (20), the next step is the collision step, which is performed using the updated density and velocity fields (ρ, u_x, u_y) given in Eqs. (21a)–(21c) and then determining the change of moments under collision $\widehat{p}_\beta(\beta = 3, 4\ldots 8)$ using Eq. (17). Then, implementing the other part of the symmetrized mass and momentum steps with using a half time step to solve Eqs. (19a) and (19b), we obtain the target density and velocity field after collision represented as (ρ^p, u_x^p, u_y^p) via $\rho^p - \rho = M^A\frac{\Delta t}{2}$, $\rho u_x^p - \rho u_x = F_x\frac{\Delta t}{2}$ and $\rho u_y^p - \rho u_y = F_y\frac{\Delta t}{2}$. Thus, we have

$$\text{Post-collision Momentum Source Step } \mathbf{F}^{1/2}: \rho u_x^p = \rho u_x + F_x\frac{\Delta t}{2}, \quad \rho u_y^p = \rho u_y + F_y\frac{\Delta t}{2}, \tag{22a}$$

$$\text{Post-collision Mass Source Step } \mathbf{M}^{1/2}: \ \rho^p = \rho + M^A\frac{\Delta t}{2}. \tag{22b}$$

By rewriting the above results for the post-collision source steps in terms of the output density ρ^o and velocity field $\mathbf{u}^o = \left(u_x^o, u_y^o\right)$ via Eqs. (21a)–(21c), we get

$$\rho^p = \rho^o + M^A\Delta t, \quad \rho u_x^p = \rho u_x^o + F_x\Delta t, \quad \rho u_y^p = \rho u_y^o + F_y\Delta t. \tag{23}$$

To effectively design the post-collision distribution function f_α^p in the cascaded LB scheme so that Eq. (23) is precisely satisfied, we consider $f_\alpha^p = f_\alpha + (\mathbf{K}\cdot\widehat{\mathbf{p}})_\alpha$ and taking its zeroth and first moments, we obtain

$$\rho^p = \Sigma_\alpha f_\alpha^p = \Sigma_\alpha f_\alpha + \Sigma_\beta\langle K_\beta|1\rangle\widehat{p}_\beta, \tag{24a}$$
$$\rho u_x^p = \Sigma_\alpha f_\alpha^p e_{\alpha x} = \Sigma_\alpha f_\alpha e_{\alpha x} + \Sigma_\beta\langle K_\beta|e_x\rangle\widehat{p}_\beta, \tag{24b}$$
$$\rho u_y^p = \Sigma_\alpha f_\alpha^p e_{\alpha y} = \Sigma_\alpha f_\alpha e_{\alpha y} + \Sigma_\beta\langle K_\beta|e_y\rangle\widehat{p}_\beta. \tag{24c}$$

Since the orthogonal basis vectors $|K_\beta\rangle$ given in Eq. (12) satisfy $\Sigma_\beta\langle K_\beta|1\rangle = 9\widehat{p}_0, \Sigma_\beta\langle K_\beta|e_x\rangle = 6\widehat{p}_1, \Sigma_\beta\langle K_\beta|e_y\rangle = 6\widehat{p}_2$, Eqs. (24a)–(24c) become

$$\rho^p = \rho^o + 9\widehat{p}_0, \quad \rho u_x^p = \rho u_x^o + 6\widehat{p}_1, \quad \rho u_y^p = \rho u_y^o + 6\widehat{p}_2. \tag{25}$$

Comparing Eqs. (23) and (25), it follows that the change of the zeroth moment ($\widehat{p}_0$) and the first moments ($\widehat{p}_1$ and $\widehat{p}_2$) due to mass and momentum sources can be written as

$$\widehat{p}_0 = \frac{M^A}{9}\Delta t, \quad \widehat{p}_1 = \frac{F_x}{6}\Delta t, \quad \widehat{p}_2 = \frac{F_y}{6}\Delta t. \tag{26}$$

where M_A follows from Eq. (4a), F_x and F_y are given in Eq. (5) and (4b) and (4c). These expressions effectively provide the desired post-collision states of the distribution function, i.e., f_α^p due to mass and momentum sources.

The overall scheme presented above based on operator splitting provides a consistent approach to represent mass and momentum sources in the fluid motion. In particular, the pre-collision steps each over a half time step length shown in Eqs. (21a)–(21c) introduce the effect of mass source and the forces into the moment equilibria of all orders before they undergo central moment relaxation (Eq. (17)). As a result, in particular, they eliminate the spurious terms such as $F_iu_j + F_ju_i$ arising in the second order non-equilibrium moments related to the viscous stress in the Chapman-Enskog analysis and correctly recover the Navier-Stokes equations [51,50]. In addition, the use of two half mass source/force steps around the collision step is consistent with the classical Strang splitting of multiple operators and is second order accurate (see [51,50] for details and also [52] for its application to a multiple relaxation formulation). An alternative approach to introduce forcing terms based on an unsplit formulation for the cascaded LB method has been presented recently in [47,48].

Thus, finally expanding $(\mathbf{K}\cdot\widehat{\mathbf{p}})_\alpha$ in Eq. (16a), the components of the post-collision distribution functions read as

$$\begin{aligned}
f_0^p &= f_0 + \left[\widehat{p}_0 - 4(\widehat{p}_3 - \widehat{p}_8)\right],\\
f_1^p &= f_1 + \left[\widehat{p}_0 + \widehat{p}_1 - \widehat{p}_3 + \widehat{p}_4 + 2(\widehat{p}_7 - \widehat{p}_8)\right],\\
f_2^p &= f_2 + \left[\widehat{p}_0 + \widehat{p}_2 - \widehat{p}_3 - \widehat{p}_4 + 2(\widehat{p}_6 - \widehat{p}_8)\right],\\
f_3^p &= f_3 + \left[\widehat{p}_0 - \widehat{p}_1 - \widehat{p}_3 + \widehat{p}_4 - 2(\widehat{p}_7 + \widehat{p}_8)\right],\\
f_4^p &= f_4 + \left[\widehat{p}_0 - \widehat{p}_2 - \widehat{p}_3 - \widehat{p}_4 - 2(\widehat{p}_6 + \widehat{p}_8)\right],\\
f_5^p &= f_5 + \left[\widehat{p}_0 + \widehat{p}_1 + \widehat{p}_2 + 2\widehat{p}_3 + \widehat{p}_5 - \widehat{p}_6 - \widehat{p}_7 + \widehat{p}_8\right],\\
f_6^p &= f_6 + \left[\widehat{p}_0 - \widehat{p}_1 + \widehat{p}_2 + 2\widehat{p}_3 - \widehat{p}_5 - \widehat{p}_6 + \widehat{p}_7 + \widehat{p}_8\right],\\
f_7^p &= f_7 + \left[\widehat{p}_0 - \widehat{p}_1 - \widehat{p}_2 + 2\widehat{p}_3 + \widehat{p}_5 + \widehat{p}_6 + \widehat{p}_7 + \widehat{p}_8\right],\\
f_8^p &= f_8 + \left[\widehat{p}_0 + \widehat{p}_1 - \widehat{p}_2 + 2\widehat{p}_3 - \widehat{p}_5 + \widehat{p}_6 - \widehat{p}_7 + \widehat{p}_8\right].
\end{aligned} \tag{27}$$

where $\widehat{p}_0, \widehat{p}_1$ and $\widehat{p}_2$ are obtained from Eq. (26) and $\widehat{p}_3, \widehat{p}_4, \cdots, \widehat{p}_8$ from Eq. (17).

2.3. Cascaded LB scheme for azimuthal velocity field: operator splitting for source term

We now construct a novel cascaded LB scheme for the solution of the equation of the azimuthal momentum component ($\psi = \rho u_\theta$) given in Eqs. (6) and (7) using a D2Q5 lattice [50]. First, defining the vectors corresponding to particle velocity components and a 5-dimensional vector $|1\rangle$ as

$$|e_x\rangle = (0, 1, 0, -1, 0)^\dagger, \tag{28a}$$
$$|e_y\rangle = (0, 0, 1, 0, -1)^\dagger, \tag{28b}$$
$$|1\rangle = (1, 1, 1, 1, 1)^\dagger, \tag{28c}$$

where taking the inner product of the distribution function g_α with $|1\rangle$ defines its zeroth moment. Using these, the five orthogonal basis vectors can be written as

$$L_0 = |1\rangle, \quad L_1 = |e_x\rangle, \quad L_2 = |e_y\rangle,$$
$$L_3 = 5\left|e_x^2 + e_y^2\right\rangle - 4|1\rangle, \quad L_4 = \left|e_x^2 - e_y^2\right\rangle, \tag{29}$$

which can be grouped together as the following transformation matrix that converts the changes in moments to those in the distribution functions:

$$\mathbf{L} = [L_0, L_1, L_2, L_3, L_4]. \tag{30}$$

In order to design a cascaded collision operator to solve for the azimuthal momentum, which acts as a passive scalar field $\psi = \rho u_\theta$ described by an advection-diffusion equation under the action of a local source term (Eqs. (6) and (7)), we define the following central moments and raw moments of the distribution function g_α and its equilibrium g_α^{eq} as

$$\begin{pmatrix} \hat{\kappa}^{\psi}_{x^m y^n} \\ \hat{\kappa}^{eq,\psi}_{x^m y^n} \end{pmatrix} = \sum_\alpha \begin{pmatrix} g_\alpha \\ g_\alpha^{eq} \end{pmatrix} (e_{\alpha x} - u_x)^m (e_{\alpha y} - u_y)^n, \tag{31}$$

and

$$\begin{pmatrix} \hat{\kappa}^{\psi'}_{x^m y^n} \\ \hat{\kappa}^{eq,\psi'}_{x^m y^n} \end{pmatrix} = \sum_\alpha \begin{pmatrix} g_\alpha \\ g_\alpha^{eq} \end{pmatrix} e^m_{\alpha x} e^n_{\alpha y}. \tag{32}$$

respectively. The central moments of the equilibrium $\hat{\kappa}^{eq,\psi}_{x^m y^n}$ are devised be equal to those for the Maxwellian after replacing the density with the scalar field in its expression. Then the cascaded collision step is written in terms of the relaxation of different central moments to their equilibria. Similar to the previous section, a symmetrized operator split scheme will now be developed to solve Eqs. (6) and (7) in the cascaded LB formulation. First, we represent the solution of Eq. (6) without the source term (Eq. (7)) through the collision and streaming steps of the distribution function g_α as

$$\textbf{Step C}: \quad g_\alpha^p = g_\alpha + \left(\mathbf{L} \cdot \widehat{\mathbf{q}}\right)_\alpha, \tag{33a}$$

$$\textbf{Step S}: \quad g_\alpha(\mathbf{x}, t) = g_\alpha^p(\mathbf{x} - \mathbf{e}_\alpha \Delta t, t). \tag{33b}$$

where g_α^p is the post-collision distribution function and $\widehat{\mathbf{q}} = (\widehat{q}_o, \widehat{q}_1, \cdots \widehat{q}_4)$ represents the changes of different moments under a cascaded collision prescribed as a relaxation process in terms of central moments, which reads as [50]

$$\begin{aligned}
\widehat{q}_1 &= \frac{\omega_1^\psi}{2}\left[\psi u_x - \widehat{\kappa}_x^{\psi'}\right], \\
\widehat{q}_2 &= \frac{\omega_2^\psi}{2}\left[\psi u_y - \widehat{\kappa}_y^{\psi'}\right], \\
\widehat{q}_3 &= \frac{\omega_3^\psi}{4}\left[2c_{s\psi}^2 - \left(\widehat{\kappa}_{xx}{}^{\psi'} + \widehat{\kappa}_{yy}^{\psi'}\right) + 2\left(u_x \widehat{\kappa}_x^{\psi'} + u_y \widehat{\kappa}_y^{\psi'}\right) \right. \\
&\quad \left. + \left(u_x^2 + u_y^2\right)\psi\right] + u_x \widehat{q}_1 + u_y \widehat{q}_2, \\
\widehat{q}_4 &= \frac{\omega_4^\psi}{4}\left[-\left(\widehat{\kappa}_{xx}{}^{\psi'} - \widehat{\kappa}_{yy}^{\psi'}\right) + 2\left(u_x \widehat{\kappa}_x^{\psi'} - u_y \widehat{\kappa}_y^{\psi'}\right) + \left(u_x^2 - u_y^2\right)\psi\right] \\
&\quad + u_x \widehat{q}_1 - u_y \widehat{q}_2,
\end{aligned} \tag{34}$$

where $\omega_1^\psi, \omega_2^\psi, \omega_3^\psi$ and ω_4^ψ are the relaxation parameters. Since ψ is conserved during collision, $\widehat{q}_o = 0$. The relaxation parameters for the first order moments (ω_1^ψ and ω_2^ψ) are related to diffusivity $D_\psi = \nu = c_{s\psi}^2\left(\frac{1}{\omega_j^\psi} - \frac{1}{2}\right)\Delta t, j = 1, 2$ where $c_{s\psi}^2$ is a free parameter, which is set to 1/3. The relaxation parameters for the higher order moments, which influence numerical stability, are taken to be unity in this study. After the streaming step in Eq. (33b), the output passive azimuthal momentum field ψ^o is computed as the zeroth moment of g_α as

$$\psi^o = \sum_\alpha^4 g_\alpha. \tag{35}$$

The source term S_ψ, which was eliminated in the above, will now be introduced by appropriately combining its effect after solution of the following such problem:

$$\textbf{Step R}: \quad \partial_t \psi = S_\psi \tag{36}$$

Its solution will now be combined with the split solution obtained in the absence of the source term in Eqs. (33a) and (33b) via a symmetric operator splitting technique over a time interval $[t, t + \Delta t]$, analogous to that considered in the previous subsection. This can be represented as

$$g_\alpha(\mathbf{x}, t + \Delta t) = \mathbf{S}\,\mathbf{R}^{1/2}\,\mathbf{C}\,\mathbf{R}^{1/2} g_\alpha(\mathbf{x}, t), \tag{37}$$

The pre-collision source step $\mathbf{R}^{1/2}$ is executed via a solution of Eq. (36) over a duration $\Delta t/2$, which yields $\psi - \psi^o = S_\psi \frac{\Delta t}{2}$, and hence

$$\text{Pre-collision Source Step } \mathbf{R}^{1/2}: \ \psi = \psi^o + S_\psi \frac{\Delta t}{2}. \tag{38}$$

Based on this updated scalar field, the changes of different moments under collision $\widehat{q}_\beta, \beta = 1, 2, 3, 4$, given in Eq. (34) can be computed. Similarly, the other part of the source step $\mathbf{R}^{1/2}$ with half time step following collision can be performed by solving Eq. (36), which can be expressed as

$$\text{Post-collision Source Step } \mathbf{R}^{1/2}: \psi^p = \psi + S_\psi \frac{\Delta t}{2}, \tag{39}$$

where ψ^p is the target scalar field after collision. By rewriting it in terms of the output scalar field ψ^o using Eq. (38), we have

$$\psi^p = \psi^o + S_\psi \Delta t. \tag{40}$$

In order for the post-collision distribution function $g_\alpha^p = g_\alpha + \left(\mathbf{L} \cdot \widehat{\mathbf{q}}\right)_\alpha$ to satisfy Eq. (40), we write its zeroth moment as

$$\psi^p = \Sigma_\alpha g_\alpha^p = \Sigma_\alpha g_\alpha + \Sigma_\beta \langle L_\beta | 1 \rangle \widehat{q}_\beta. \tag{41}$$

Since $\Sigma_\beta \langle L_\beta | 1 \rangle q_\beta = 5\widehat{q}_o$ via orthogonal of basis vectors (see Eq. (29)), it follows from Eqs. (35) and (41) that $\psi^p = \psi^o + 5\widehat{q}_0$. Comparing this with Eq. (40), we get the change of the zeroth moment $\widehat{q}_o$ due to the presence of the source term S_ψ as

$$\widehat{q}_0 = \frac{S_\psi}{5}\Delta t. \tag{42}$$

The modeling of the source term for the transport of a scalar field via the above operator splitting approach provides a consistent representation of their effect in the convection-diffusion equation. This is due to the fact that the use of the pre-collision source step over a half time step (Eq. (38)) introduces the effect of the scalar source term into the moment equilibria of all orders before they participate in the collision step via the relaxation of various central moments (Eq. (34)). Moreover, the symmetric application of pre- and post-collision source steps over a half time step length in each case makes it consistent with the Strang splitting [50]. Similar considerations hold for the strategy for including the local heat sources presented in the next section. Another equivalent approach based on an unsplit formulation to incorporate the source term for the scalar field is discussed in [49].

Finally, the components of the post-collision distribution function in Eq. (33a) can be expressed after expanding $\left(\mathbf{L} \cdot \widehat{\mathbf{q}}\right)_\alpha$ as

$$\begin{aligned}
g_0^p &= g_0 + \left[\widehat{q}_0 - 4\widehat{q}_3\right], \\
g_1^p &= g_1 + \left[\widehat{q}_0 + \widehat{q}_1 + \widehat{q}_3 + \widehat{q}_4\right], \\
g_2^p &= g_2 + \left[\widehat{q}_0 + \widehat{q}_2 + \widehat{q}_3 - \widehat{q}_4\right], \\
g_3^p &= g_3 + \left[\widehat{q}_0 - \widehat{q}_1 + \widehat{q}_3 + \widehat{q}_4\right], \\
g_4^p &= g_4 + \left[\widehat{q}_0 - \widehat{q}_2 + \widehat{q}_3 - \widehat{q}_4\right],
\end{aligned} \tag{43}$$

where $\widehat{q}_o$ (i.e., the change of the zeroth moment due to source) is given in Eq. (42) and $\widehat{q}_\beta, \beta = 1, 2, 3, 4$ (i.e., the changes of the higher, non-conserved, moments under collision) is obtained from Eq. (34).

2.4. Cascaded LB scheme for temperature field: operator splitting for source term

As in the previous section, we consider a D2Q5 lattice, and use the orthogonal basis vectors L_β and the transformation matrix $\mathbf{L}$ given in Eqs. (29) and (30), respectively, to design a cascaded LB scheme for the solution of the temperature field $\phi = T$. Its evolution is presented by the advection-diffusion equation with a source term given in Eqs. (8) and (9). The various central moments and raw moments of the corresponding distribution function h_α and its equilibrium h_α^{eq} are defined as

$$\begin{pmatrix} \hat{\kappa}^{\phi}_{x^m y^n} \\ \hat{\kappa}^{eq,\phi}_{x^m y^n} \end{pmatrix} = \sum_\alpha \begin{pmatrix} h_\alpha \\ h_\alpha^{eq} \end{pmatrix} (e_{\alpha x} - u_x)^m (e_{\alpha y} - u_y)^n, \tag{44}$$

and

$$\begin{pmatrix} \hat{\kappa}^{\phi'}_{x^m y^n} \\ \hat{\kappa}^{eq,\phi'}_{x^m y^n} \end{pmatrix} = \sum_\alpha \begin{pmatrix} h_\alpha \\ h_\alpha^{eq} \end{pmatrix} e^m_{\alpha x} e^n_{\alpha y}. \tag{45}$$

As before, we use the symmetrized operator splitting to include the source term S_ϕ in the cascaded LB scheme, which can be presented as:

$$h_\alpha(\mathbf{x}, t + \Delta t) = \mathbf{S}\mathbf{R}^{1/2}\mathbf{C}\mathbf{R}^{1/2} h_\alpha(\mathbf{x}, t), \tag{46}$$

where $\mathbf{C}$ and $\mathbf{S}$ denote the collision and streaming steps, respectively, of h_α used to solve Eq. (8) (without S_ϕ)

$$\textbf{Step C}: \; h^p_\alpha = h_\alpha + \left(\mathbf{L}\cdot\hat{\mathbf{r}}\right)_\alpha, \tag{47a}$$

$$\textbf{Step S}: \; h_\alpha(\mathbf{x}, t) = h^p_\alpha(\mathbf{x} - \mathbf{e}_\alpha \Delta t, t). \tag{47b}$$

Here, h^p_α is the post-collision distribution function and $\hat{\mathbf{r}} = (\hat{r}_o, \hat{r}_1, \hat{r}_2, \hat{r}_3, \hat{r}_4)$ is the change of different moments under collision, with $\hat{r}_o = 0$ due to ϕ being a collision invariant. In the above, after the streaming step, the solution of the output scalar field ϕ^o is computed via the zeroth moment of h_α as

$$\phi^o = \sum_{\alpha=0}^{4} h_\alpha. \tag{48}$$

The operator $\mathbf{R}^{1/2}$ applied twice in Eq. (46) represents the split solution of the scalar field due to the source term of the evolution equation $\partial_t \phi = S_\phi$ before and after collision over a half time step $\Delta t/2$. Thus, the pre-collision source step can be expressed as

$$\text{Pre-collision Source Step } \mathbf{R}^{1/2}: \phi = \phi^o + \frac{S_\phi}{2}\Delta t. \tag{49}$$

This updated scalar field ϕ is then used to compute the changes of different moments under collision $\hat{r}_\beta, \beta = 1, 2, 3, 4$, which can be written as

$$\begin{aligned}
\hat{r}_1 &= \frac{\omega_1^\phi}{2}\left[\phi u_x - \hat{\kappa}_x^{\phi'}\right], \\
\hat{r}_2 &= \frac{\omega_2^\phi}{2}\left[\phi u_y - \hat{\kappa}_y^{\phi'}\right], \\
\hat{r}_3 &= \frac{\omega_3^\phi}{4}\left[2c_s^2\phi - \left(\hat{\kappa}_{xx}{}^{\phi'} + \hat{\kappa}_{yy}^{\phi'}\right) + 2\left(u_x\hat{\kappa}_x^{\phi'} + u_y\hat{\kappa}_y^{\phi'}\right) + \left(u_x^2 + u_y^2\right)\phi\right] \\
&\quad + u_x\hat{r}_1 + u_y\hat{r}_2, \\
\hat{r}_4 &= \frac{\omega_4^\phi}{4}\left[-\left(\hat{\kappa}_{xx}^{\phi'} - \hat{\kappa}_{yy}^{\prime\phi}\right) + 2\left(u_x\hat{\kappa}_x^{\phi'} - u_y\hat{\kappa}_y^{\phi'}\right) + \left(u_x^2 - u_y^2\right)\phi\right] \\
&\quad + u_x\hat{r}_1 - u_y\hat{r}_2,
\end{aligned} \tag{50}$$

where the relaxation parameters ω_1^ϕ and ω_2^ϕ are related to the thermal diffusivity D_ϕ via $D_\phi = c_{s\phi}^2\left(\frac{1}{\omega_j^\phi} - \frac{1}{2}\right)\Delta t, j = 1, 2$, where $c_{s\phi}^2 = \frac{1}{3}$ and $\omega_3^\phi = \omega_4^\phi = 1$ in this work. Following this, the post-collision source step $\mathbf{R}^{1/2}$ can be represented as

$$\text{Post-collision Source Step } \mathbf{R}^{1/2}: \phi^p = \phi + \frac{S_\phi}{2}\Delta t, \tag{51}$$

where ϕ^p is the target scalar field following collision, which via Eq. (49) reads as $\phi^p = \phi^o + S_\phi \Delta t$. The post-collision distribution function $h^p_\alpha = h_\alpha + \left(\mathbf{L}\cdot\hat{\mathbf{r}}\right)_\alpha$ can be made to satisfy this condition using Eq. (48) and using $\Sigma_\beta \langle L_\beta | 1\rangle \hat{r}_\beta = 5\hat{r}_0$ after taking its zeroth moment, i.e., $\phi^p = \sum_\alpha h^p_\alpha$. This provides the following zeroth moment change due to S_ϕ after collision

$$\hat{r}_0 = \frac{S_\phi}{5}\Delta t. \tag{52}$$

Finally, the post-collision distribution function h^p_α can be explicitly written after expanding $\left(\mathbf{L}\cdot\hat{\mathbf{r}}\right)_\alpha$ in Eq. (47a) as follows:

$$\begin{aligned}
h_0^p &= h_0 + \left[\hat{r}_0 - 4\hat{r}_3\right], \\
h_1^p &= h_1 + \left[\hat{r}_0 + \hat{r}_1 + \hat{r}_3 + \hat{r}_4\right], \\
h_2^p &= h_2 + \left[\hat{r}_0 + \hat{r}_2 + \hat{r}_3 - \hat{r}_4\right], \\
h_3^p &= h_3 + \left[\hat{r}_0 - \hat{r}_1 + \hat{r}_3 + \hat{r}_4\right], \\
h_4^p &= h_4 + \left[\hat{r}_0 - \hat{r}_2 + \hat{r}_3 - \hat{r}_4\right],
\end{aligned} \tag{53}$$

where $\hat{r}_o$ is obtained form Eq. (52) and $\hat{r}_\beta, \beta = 1, 2, 3$ and 4, follows from Eq. (50) due to various non-conserved moment changes under collision.

3. Results and discussion

In this section, the cascaded LB schemes described above will be applied to and studied for different complex flow benchmark problems to validate them for simulations of axisymmetric flows with heat transfer and including rotational/swirling effects. These include the following: (a) Taylor-Couette flow between two rotating circular cylinders, (b) natural convection in an annulus between two stationary coaxial vertical cylinders, (c) Rayleigh-Benard convection inside vertical cylinder heated at the bottom and cooled at the top, (d) cylindrical cavity flow driven by the motion of the top lid, (e) mixed convection in a slender vertical annulus subjected to the inner cylinder rotation, and (f) melt flow in a cylinder during Czochralski crystal growth process.

3.1. Taylor-Couette flow

As the first test problem, the classical shear-driven circular Couette flow between two circular cylinders is considered [53]. This problem is used to assess the cascaded LB scheme for the azimuthal velocity component u_θ given in Section 2.3, whose evolution is represented by Eqs. (6) and (7). The radii of the inner and outer cylinders are defined as R_i and R_o, respectively. Let the angular velocities of the inner and outer cylinders be Ω_i and Ω_o, respectively, which induce an azimuthal flow within their annulus gap. The analytical solution for such a cylindrical Couette flow is given in terms of the radial variation of the azimuthal velocity as follows:

$$u_\theta(r) = Ar + \frac{B}{r},$$

where $A = \frac{\Omega_o R_o^2 - \Omega_i R_i^2}{R_o^2 - R_i^2}$, $B = \frac{(\Omega_i - \Omega_o) R_i^2 R_o^2}{R_o^2 - R_i^2}$. Here, r is the radial distance from the cylindrical axis. For ease of representation, this can be written in a non-dimensional form as

$$\frac{u_\theta(r)}{u_o} = \frac{1}{1 - \beta^2}\left[\left(\kappa - \beta^2\right)\frac{r}{R_i} + \frac{R_i}{r}(1 - \kappa)\right],$$

where $u_o = \Omega_i R_i, \beta$ is the radius ratio given by $\beta = R_i/R_o$ and κ denotes the angular velocity ratio, i.e., $\kappa = \Omega_o/\Omega_i$.

In our simulation, periodic boundary conditions are applied in the axial direction and the values of the azimuthal velocities at the inner and outer cylinder are prescribed as $u_\theta(r = R_i) = \Omega_i R_i = u_o$ and $u_\theta(r = R_o) = \Omega_o R_o = \frac{\kappa}{\beta} u_o$, respectively using the Dirichlet boundary condition implementation scheme associated with the advection-diffusion equation representing the dynamics of u_θ [54]. The outer cylinder radius is resolved by 200 lattice nodes and the lattice location for the inner cylinder is fixed using $R_i = \beta R_o$ for different choices of β. The periodic axial direction is discretized using 3 lattice nodes. The relaxation times in the cascaded LB scheme representing the kinematic shear viscosity are set as $\omega_j = 1/\tau, j = 4, 5$, where $\tau = 0.6$, and u_o is chosen such that the rotational Reynolds number $Re = u_o R_i/\nu$ becomes 5. Fig. 1 presents a comparison of the velocity profiles computed using the cascaded LB scheme against the analytical solution at the angular velocity ratio $\kappa = 0.1$ for various values of the radius ratio β ($\beta = 0.103, 0.203, 0.303$ and 0.503). It is clear that the agreement between the numerical and analytical solution is very good.

3.1.1. Order of accuracy

We will now examine our new axisymmetric cascaded LB scheme for this benchmark problem to establish its order of accuracy. In this regard, we consider the diffusive scaling, i.e., an increase in the grid resolution is accompanied by a proportional decrease in the Mach number at a fixed viscosity or a fixed relaxation time, which corresponds to an asymptotic convergence to the incompressible flow limit. For this purpose, the global relative error ($E_{g,u}$) is defined as follows:

$$E_{g,u} = \sqrt{\frac{\Sigma(u_c - u_a)^2}{\Sigma(u_a)^2}}, \tag{54}$$

where u_c is the numerical velocity field computed using the axisymmetric cascaded LB scheme and u_a is the analytical solution given above, and the summation is carried out for the whole domain. We consider fixed values of the Reynolds number $Re = 5$, radius ratio $\beta = 1/3$, relaxation time that determines the momentum diffusivity, i.e., the viscosity, to be $\tau = 0.6$. Four different grid resolutions of $24 \times 3, 48 \times 3, 96 \times 3$, and 192×3 are considered and the corresponding relative errors are computed. As displayed in Fig. 2, the global relative errors have a slope of -2.0 in the log-log scale, and thus evidently our axisymmetric cascaded LB scheme is second order accurate.

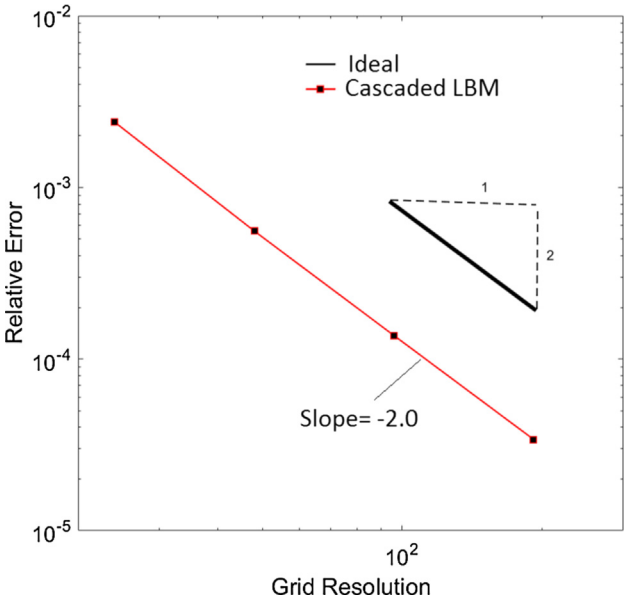

Fig. 2. Evaluation of order of accuracy for Taylor-Couette flow with a constant Reynolds number $Re = 5$, radius ratio $\beta = 1/3$ and relaxation time $\tau = 0.6$ at different grid resolutions computed using the axisymmetric cascaded LB scheme.

3.2. Natural convection in an annulus between two coaxial vertical cylinders

In order to validate our cascaded LB schemes for axisymmetric flows with heat transfer, we simulate a buoyancy-driven flow between two coaxial stationary cylinders, which is a prototype problem of both fundamental and practical interest. Since the flow field is coupled to the temperature field via the buoyancy force in view of Eqs. (3a)–(3c), (4a)–(4c), (5), (8) and (9), this problem

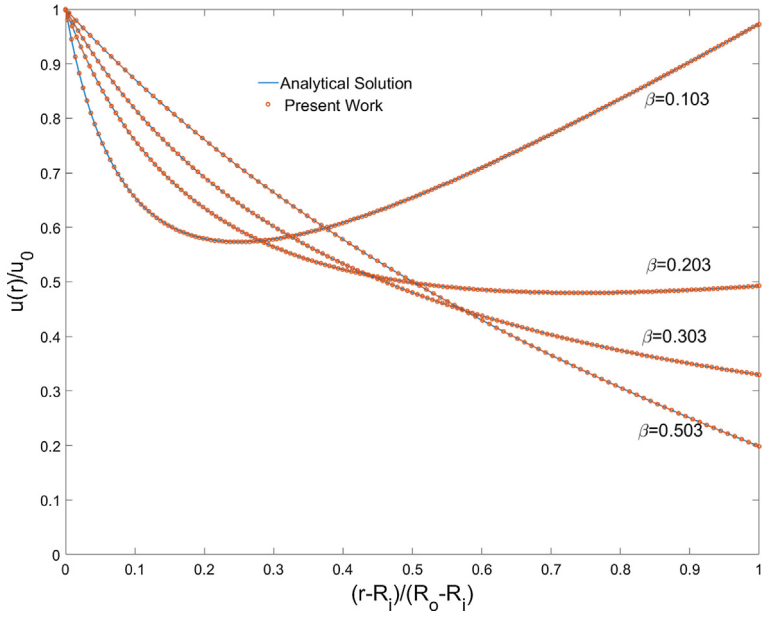

Fig. 1. Comparison between the analytical velocity profile (solid lines) and the cascaded LB solution (symbols) for the Taylor-Couette flow between two circular cylinders at an angular velocity ratio $\kappa = 0.1$ and for various values of the radius ratio β.

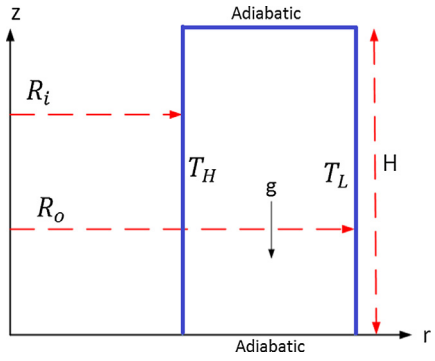

Fig. 3. Schematic illustration of the geometry and boundary conditions for natural convection in a vertical annulus.

facilitates a thorough examination of the efficacy of the coupling between the cascaded LB schemes presented in Section 2.2 and 2.4. A schematic of this problem is depicted in Fig. 3, where R_i, R_o, H and g are the radii of the inner cylinder and the outer cylinder, the height of the cylinder and the gravitation acceleration, respectively.

For the velocity field, no-slip boundary conditions are considered on all four walls involving the inner and outer cylindrical surfaces, and top and bottom walls. The inner and outer walls of the lateral cylindrical side walls are maintained at temperatures of T_H and T_L, respectively, where $T_H > T_L$, while the top and bottom walls are considered to be thermally insulated (adiabatic). As a result, this generates a body force due to buoyancy in the axial direction, which under the Boussinesq approximation, can be written as $g\beta(T - T_o)$, where β is the thermal expansion coefficient, and $T_o = (T_H + T_L)/2$. This body force component is added to the geometric source terms in Eq. (5) for F_x^b, which then sets up natural convection within the annulus of the axisymmetric geometry. This thermally driven flow problem is characterized by two dimensionless numbers, viz., the Rayleigh number Ra and Prandtl number Pr defined as

$$Ra = \frac{g\beta(T_H - T_L)L^3}{\alpha\nu}, \quad Pr = \frac{\nu}{\alpha},$$

where $L = R_o - R_i$ is the annual gap serving as the characteristic length, and ν and α are the kinematic viscosity and thermal diffusivity, respectively. In addition, the geometric parameters influencing this problem are the aspect ratio H/L and the radius ratio R_o/R_i, both of which are set to 2 in the present study. The no-slip conditions for the velocity field are implemented using the standard half-way bounce back scheme in the cascaded LB method, while the imposed temperature and no heat flux conditions on the boundaries are represented using the approach presented in [54]. All the spatial derivatives needed in the source terms in Eqs. (4b), (4c) and (9) are computed using a central difference scheme. The characteristic velocity due to natural convection $\sqrt{g\beta(T_H - T_L)R_i}$ is kept small so that the flow can be regarded as incompressible. We performed simulations at $Pr = 0.7$ and $Ra = 10^3, 10^4$ and 10^5 corresponding to the parameter spaces considered in prior studies [55,56,29]. In addition, we have also performed additional simulations at higher

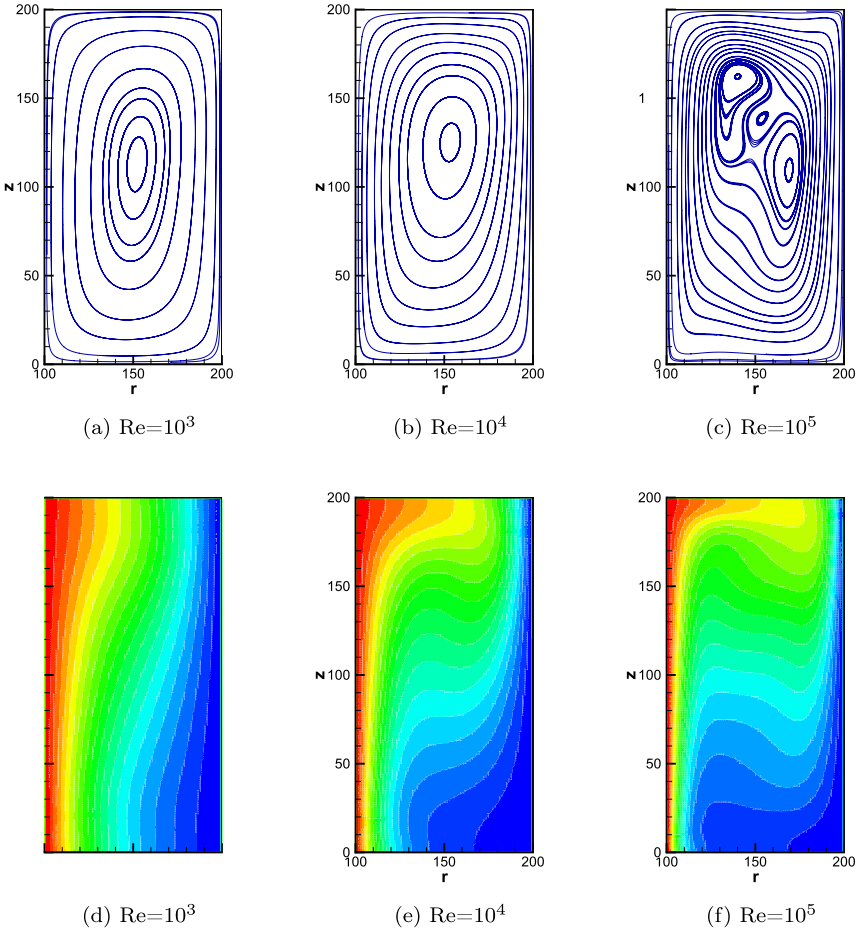

Fig. 4. Streamlines and isotherms for the natural convection between two co-axial vertical cylinders at $Pr = 0.7$ and (a, d) $Ra = 10^3$, (b, e) $Ra = 10^4$ and (c, f) $Ra = 10^5$ computed using cascaded LB schemes. Top row presents streamlines and the bottom row the isotherms.

Rayleigh numbers of $Ra = 10^6$ and $Ra = 10^7$ that could serve as possible reference results for future research work in this area. The computational domain is resolved using a grid resolution of 200×200 in the axial and radial directions, respectively, for the lower Rayleigh number cases (i.e., $Ra = 10^3, 10^4$ and 10^5) and using 300×300 for higher Rayleigh number considered (i.e., $Ra = 10^6$ and $Ra = 10^7$).

Fig. 4 presents the computed streamlines and isotherms for three different $Ra = 10^3, 10^4$ and 10^5. It is clear that as Ra increases, the vortical patterns turn to be progressively more complex, with the $Ra = 10^5$ case generating additional pairs of vortices around the middle of the annulus. Furthermore, as Ra increase, the isotherms are greatly distorted, and the velocity and thermal boundary layers become thinner near the hot and cold lateral walls signifying the strengthened convection mode of heat transfer. It may be noted that all these observations are consistent with prior studies based on other numerical methods (e.g., [55,56,29]). Furthermore, the results for the computed streamlines and the isotherms at the higher $Ra = 10^6$ and $Ra = 10^7$ are presented in Fig. 5. It can be seen that the streamline patterns become more complex, with the resulting buoyancy-driven convection becoming more intense. Also, as can be expected from scaling arguments, the thermal boundary layers near the cylinder walls become thinner thereby monotonically increasing the heat transfer rate for these higher Ra cases.

Then in order to quantify the rates of heat transfer on the lateral walls, the overall Nusselt numbers Nu_i and Nu_o on the inner and outer cylinders can be defined as

$$Nu_i = \frac{-R_i}{H(T_H - T_L)} \int_o^H (\partial_y T)_i dx, \quad Nu_o = \frac{-R_o}{H(T_H - T_L)} \int_o^H (\partial_y T)_o dx,$$

and hence the average Nusselt number $\overline{Nu} = (Nu_i + Nu_o)/2$.

First, we have conducted grid sensitivity analysis to identify the minimum grid resolution necessary to provide converged heat transfer rate results for each Rayleigh number. For example, Table 1 reports the results of a grid convergence test in terms of the average Nusselt number $\overline{Nu}$ for a typical $Ra = 10^4$ by repeating the simulations for three different mesh resolutions of $100 \times 100, 200 \times 200, 250 \times 250$. From this table, it can be seen that for this benchmark problem, while the $\overline{Nu}$ results between the grid resolution cases 100×100 and 200×200 cases vary appreciably, that between 200×200 and 250×250 show relatively negligible variations. Hence, the results with using 200×200 can be deemed to have shown grid convergence for $Ra = 10^4$. In a similar manner, we have performed a sensitivity study and established the grid convergence for various Ra for different benchmark problems.

Table 2 shows a comparison of the average Nusselt number computed using the cascaded LB scheme for $Ra = 10^3, 10^4$, and 10^5 against prior numerical benchmark results [55,56,29]. It can be seen that our predictions for the average Nusselt numbers agree well with those obtained by other methods. In addition, this table also includes new results for the higher Ra of 10^6 and 10^7. It is evident that increasing the Rayleigh number increases the average Nusselt number. For example, the heat transfer rate increases by about six times when Ra increases from 10^4 to 10^7. The new quantitative data for $\overline{Nu}$ for $Ra = 10^6$ and 10^7, in particular, could serve as possible benchmark results for future research work.

3.3. Rayleigh-Benard convection in a circular vertical cylinder

We now demonstrate the ability of our axisymmetric cascaded LB schemes to simulate Rayleigh-Benard convection in a vertical cylinder, which is classical thermally-driven flow and has been well studied experimentally and using conventional numerical methods (e.g. [57,5]). Here, the fluid is heated from below, where the bottom wall is at a temperature T_H while the top wall is kept at a lower temperature T_L and the lateral wall of a cylinder of radius R and height H is maintained to be adiabatic (see Fig. 6). As a result of the buoyancy force generated, this sets up natural convection currents, whose dynamics is governed by the Rayleigh

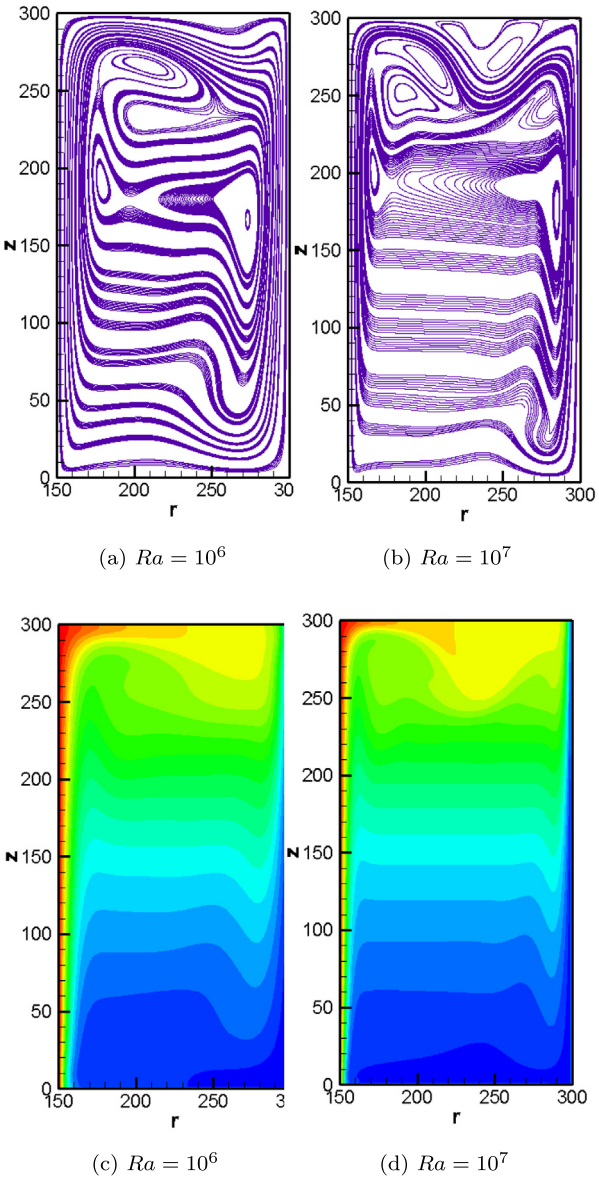

Fig. 5. Streamlines and isotherms for the natural convection between two co-axial vertical cylinders at $Pr = 0.7$ and (a, c) $Ra = 10^6$, (b, d) $Ra = 10^7$ computed using cascaded LB schemes. Top row presents streamlines and the bottom row the isotherms. Grid resolution used is 300×300.

Table 1
Grid convergence study given in terms of the average Nusselt number $\overline{Nu}$ for $Ra = 10^4$ for natural convection in a cylindrical annulus computed using axisymmetric cascaded LB schemes.

Grid Resolution	$\overline{Nu}$
100×100	3.172
200×200	3.199
250×250	3.202

Table 2
Comparison of the average Nusselt number $\overline{Nu}$ for different Ra for natural convection in a cylindrical annulus computed using axisymmetric cascaded LB schemes with other reference numerical solutions and new results for $Ra = 10^6$ and 10^7.

Ra	Cascaded LB schemes	Ref. [55]	Ref. [56]	Ref. [29]
10^3	1.688	–	–	1.692
10^4	3.199	3.037	3.163	3.215
10^5	5.781	5.760	5.882	5.798
10^6	10.421	–	–	–
10^7	18.411	–	–	–

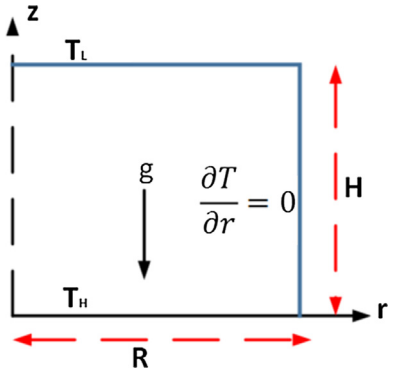

Fig. 6. Schematic illustration of Rayleigh-Benard Convection in a vertical cylinder.

number $Ra = g\beta(T_H - T_L)H^3/(\alpha\nu)$, Prandtl number, $Pr = \nu/\alpha$ and the cylinder aspect ratio $R_A = H/R$. For the purpose of validating the novel LB schemes presented in this work, we set $Pr = 0.7, Ra = 5 \times 10^3$ and $R_A = 1$ and the domain is resolved by 100×100 lattice nodes by using the relaxation times $\omega_j = 1/\tau, j = 4, 5$, where $\tau = 0.85$. No slip, and constant temperature and adiabatic boundary conditions are represented by using the same approaches are mentioned earlier, and the axis of symmetry is taken into account by using the mirror boundary conditions for the particle distribution functions in the LB schemes.

Fig. 7 show the steady isotherms and velocity vectors. Interestingly, it can be seen that based on the initial conditions for temperature, different flow patterns and isotherms are observed. In particular, if the initial temperature is set to T_L everywhere, an up flow draft around the center of the cylinder is observed, while if a higher buoyancy force is prescribed by the initial conditions, a down flow convective current around the center of the cylinder is set up. These reversal in flow patterns are consistent with findings based on other numerical schemes [27,5].

In addition, Table 3 presents a comparison of the maximum velocity in dimensionless form using the natural convection velocity scale $\sqrt{g\beta H(T_H - T_L)}$ obtained using axisymmetric cascaded LB approach with the results from the work of [27,5]. Evidently, the computed results agree very well with those reported in the literature.

Table 3
Comparison of the dimensionless maximum velocity obtained using the scale $\sqrt{g\beta H(T_H - T_L)}$ for Rayleigh-Benard convection in a vertical cylinder at $Ra = 5 \times 10^3$ computed using axisymmetric cascaded LB schemes with reference data.

Ra	Reference	Up-flow	Down-flow
5×10^3	Ref. [27]	0.353	0.351
	Ref. [5]	0.353	0.353
	Present work	0.353	0.351

3.4. Swirling flow in a lid-driven cylindrical container

In this section, we investigate the ability of the axisymmetric cascaded LB schemes to accurately simulate the dominant role played by the swirling motion and its coupling with the complex radial and axial flow induced in the meridian plane. In this regard, we consider the symmetry breaking flow in a cylindrical container of radius R and height H driven by a rotating top end wall at angular velocity Ω (see Fig. 8).

The dynamics of this flow is presented by Eqs. (3a)–(3c), (4a)–(4c), (6) and (7), whose solution scheme via our cascaded LB formulation is presented in Section 2.2 and 2.3. Briefly, as the fluid in the vicinity of the top lid gains azimuthal motion, it is ejected radially outward, and then downward due to the constraining effect of the side wall. Subsequently as the fluid reaches the bottom it is pushed radially inward, and when it is closer to the axis, it travels upward, thereby completing flow circulation in the meridian plane. The details of the physics and the flow pattern depend on the aspect ratio $R_A = H/R$ and the rotational Reynolds number $Re = R^2\Omega/\nu$. Various experiments (e.g., [58,59]) and numerical simulations (e.g., [60–62]) have revealed that for certain combinations of the characteristic parameters R_A and Re, distinct recirculation region around the cylinder axis, designated as the vortex breakdown bubble, may occur. For example, Refs. [59,63] show that for cases (R_A, Re) equal to (1.5, 990) and (2.5,1010), no vortex breakdown bubbles occur whereas for (1.5, 1290), they do occur.

In order to asses and validate our cascaded LB schemes presented earlier to simulate such complex swirling flow, we consider the following four test cases: $Re = 990$ and $Re = 1290$ with $R_A = 1.5$ and $Re = 1010$ and $Re = 2020$ with $R_A = 2.5$. The computational domain is resolved using a mesh resolution of 100×150 for $R_A = 1.5$ and 100×250 for $R_A = 2.5$. No-slip boundary conditions are used at bottom, lateral and top walls: $u_\theta = u_r = u_z = 0$ at $z = 0$ and $r = R$, and $u_\theta = r\Omega, u_r = u_z = 0$ at $z = H$. The streamlines computed using the cascaded LB schemes for the above four cases are in Fig. 9. It can be seen that no vortex break-down

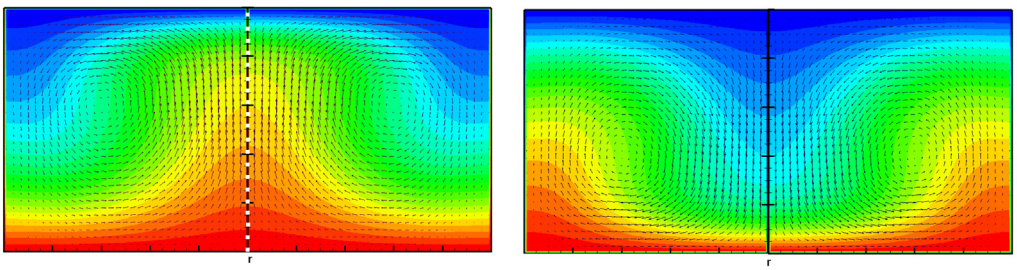

(a) Up-flow (b) Down-flow

Fig. 7. Isotherms and velocity vectors for Rayleigh-Benard convection in a vertical cylinder at $Ra = 5 \times 10^3$, $Pr = 0.7$, $R_A = 1$. Left column: Up-flow pattern and Right column: Down-flow pattern.

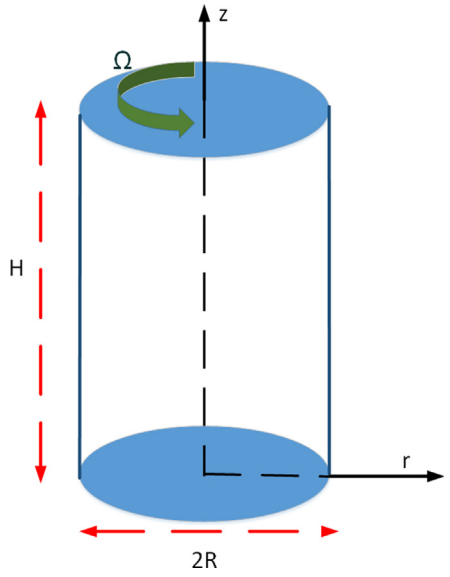

Fig. 8. Schematic of swirling flow in a confined cylinder driven by a rotating top lid.

bubbles appear for (R_A, Re) equal to (1.5, 990) and (2.5, 1010). On the other hand, one vortex break down bubble is seen at (1.5, 1290) and two break down bubbles occur in the vicinity of the cylinder axis at (2.5, 2200). These distinct regimes in swirling flows and the complex flow structure for different (R_A, Re) cases are strikingly consistent with prior numerical solution (e.g., [63,20,22,64]). Quantitative comparison of the computed structure of the axial velocities along the axis of symmetry obtained using the axisymmetric cascaded LB schemes for the above four sets of the aspect ratios R_A and Reynolds numbers Re against the results from a NS-based solver (given in [63]) are shown in Fig. 10. Here, the axial velocity is scaled by the maximum imposed azimuthal velocity $u_o = \Omega R$ on the rotating lid and the axial distance z by the cylinder height H. The numerical results of our central moments based cascaded LB method for the axial velocity profiles are in very good agrement with the NS-based solution approach [63]. Also, in particular, notice local negative values for the axial velocities for the cases $Re = 1290$ and $R_A = 1.5$ and $Re = 2200$ and $R_A = 2.5$, which is an indication of the presence of one or more vortex breakdown bubbles. As such, both the magnitudes and the shapes of the axial velocity distributions are well reproduced by our cascaded LB approach using operator splitting to represent complex flows in cylindrical coordinates.

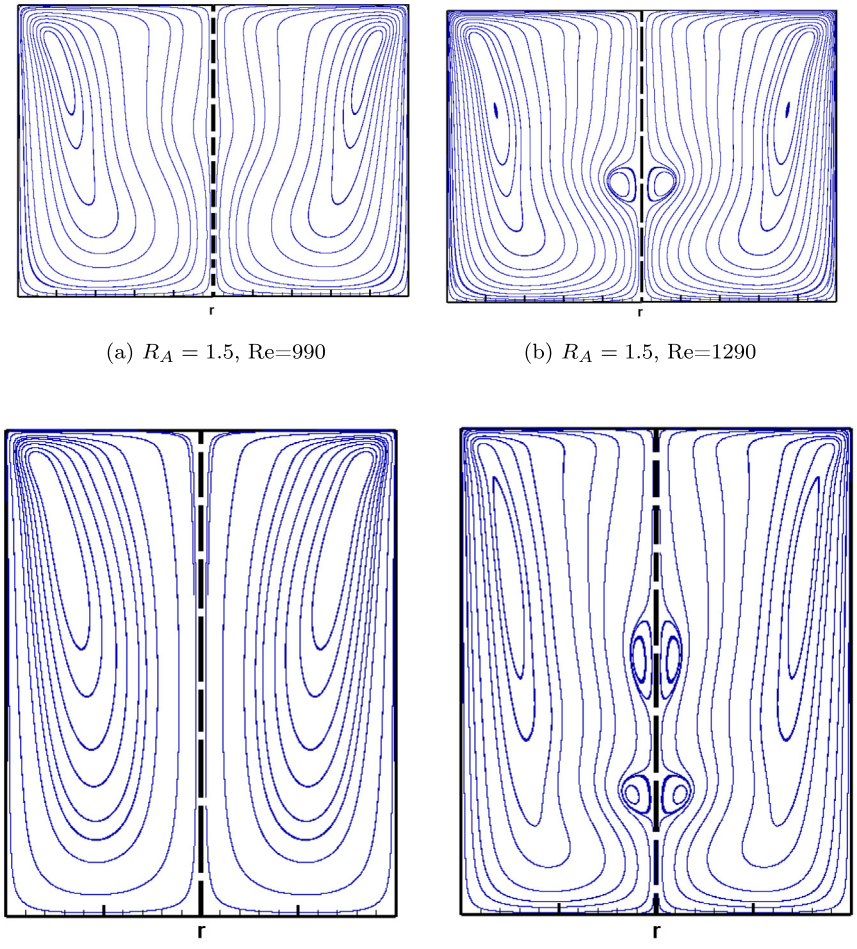

(a) $R_A = 1.5$, Re=990 (b) $R_A = 1.5$, Re=1290

(c) $R_A = 2.5$, Re=1010 (d) $R_A = 2.5$, Re=2200

Fig. 9. Computed streamline patterns in the meridian plane due to swirling flow in a confined cylinder driven by a rotating lid at various aspect ratios and Reynolds numbers using the axisymmetric cascaded LB sachems: (a) $R_A = 1.5$ and $Re = 990$, (b) $R_A = 1.5$ and $Re = 1290$ (c)$R_A = 2.5$ and $Re = 1010$ and (d)$R_A = 2.5$ and $Re = 2200$.

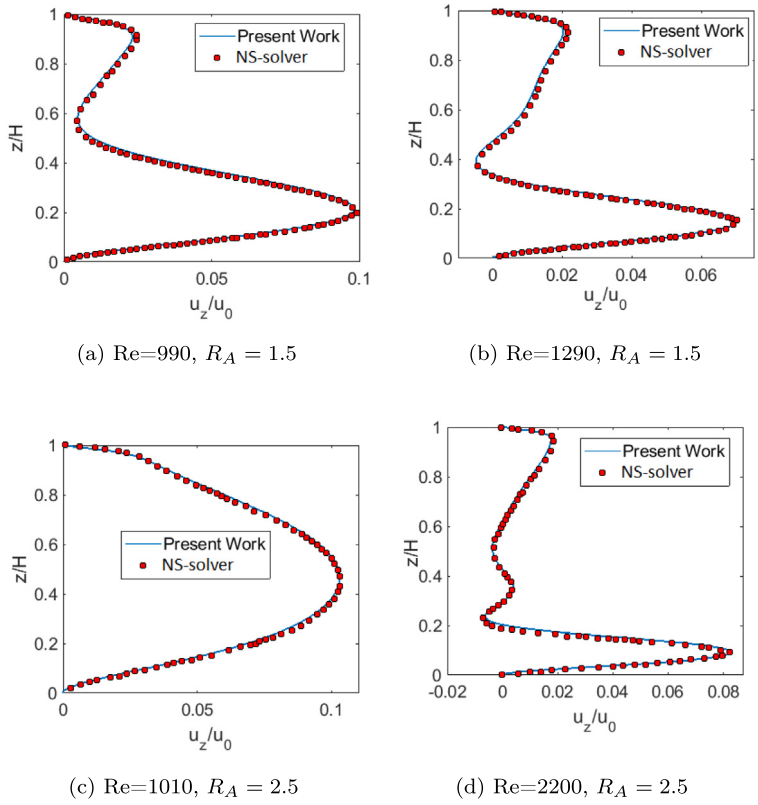

(a) Re=990, $R_A = 1.5$ (b) Re=1290, $R_A = 1.5$

(c) Re=1010, $R_A = 2.5$ (d) Re=2200, $R_A = 2.5$

Fig. 10. Dimensionless axial velocity profile u_z/u_o as a function of the dimensional axial distance z/H for (a) $R_A = 1.5$ and $Re = 990$, (b) $R_A = 1.5$ and $Re = 1290$ (c)$R_A = 2.5$ and $Re = 1010$ and (d)$R_A = 2.5$ and $Re = 2200$: Comparison between axisymmetric cascaded LB scheme predictions and NS-based solver results ([63]).

3.5. Mixed convection in a slender vertical annulus between two coaxial cylinders

We will now assess our new axisymmetric LB computational approach based on central moments to simulate the combined effects of rotation and buoyancy forces on the flow and heat transfer in confined cylindrical spaces. In this regard, we investigate mixed convection in a slender vertical annulus between two coaxial cylinders arising due to inner side wall rotation, which has numerous applications related to rotating machinery and various other heat transfer systems. This problem involving both natural convection and forced convection due to rotation can test all the three axisymmetric cascaded LB formulations (Sections 2.2–2.4) in a unified manner.

A schematic arrangement of this axisymmetric thermal flow problem is shown in Fig. 11. It consist of two coaxial cylinders of height H, with an annular gap $D = R_o - R_i$, where R_i and R_o are the radii of the inner and outer cylinders, respectively. The lateral walls of the inner and outer cylinders are maintained at temperatures T_H and T_L, respectively, where $T_H > T_L$, and their bottom and top ends are thermally insulated. The inner cylinder is subjected to rotation at an angular velocity Ω_i, while the outer cylinder and the end walls are considered to be rigidly fixed. As noted in a recent study [31], this problem is governed by the following characteristic dimensionless parameters: Prandtl number $Pr = \nu/\alpha$, radius ratio $R_{io} = R_o/R_i$ slenderness ratio $\eta = H/(R_o - R_i)$, Reynolds number $Re = \Omega_i R_i D/\nu$, Grashof number $Gr = g\beta(T_H - T_L)D^3/\nu^2$, and $\sigma = Gr/Re^2$, where the parameter σ is used to measure the strength of the buoyancy force relative to the centrifugal force. Hence, σ characterizes the degree of mixed convection.

In the present study, we set $Pr = 0.7, R_{io} = 2, \eta = 10, Re = 100$, and three cases of σ are considered: $\sigma = 0, 0.01$ and 0.05. The grid

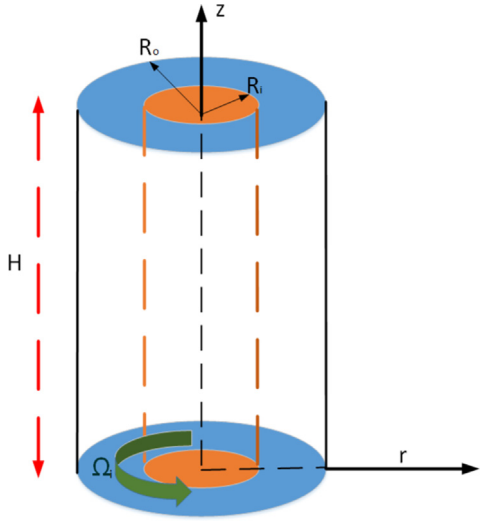

Fig. 11. Schematic of the arrangement for mixed convection in a slender cylindrical annulus with inner lateral wall rotation.

resolution used for all the three cases is 40×400, in which the location of the inner cylinder from the axis R_i is at 40. Fig. 12 shows the computed contours of the azimuthal velocity, temperature field, vorticity and streamlines for the above three values of σ. When $\sigma = 0$, there is no buoyancy force and the flow and the temperature fields are influenced by the centrifugal force and the forced convection effects, which manifest in the form of five pairs of counter-rotating cells, viz., the classical Taylor vortex cells arising from centrifugal flow instability between curved walls [2]. As σ is increased, the presence of buoyancy forces and the associated

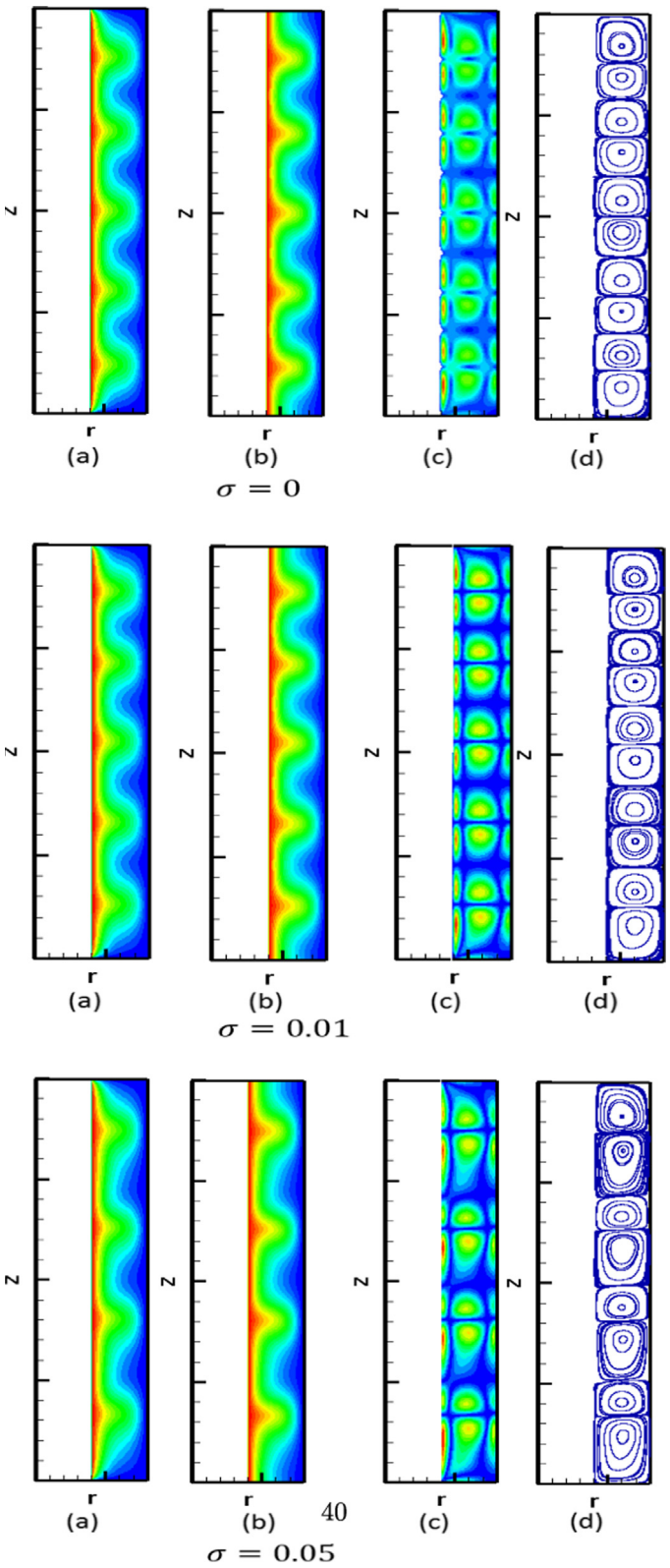

Fig. 12. Contours of (a) azimuthal velocity, (b) temperature, (c) vorticity, and (d) streamlines for mixed convection in a slender cylindrical annulus for three different values of σ computed using the axisymmetric cascaded LB schemes.

natural convective fluid currents alter the overall flow structure and the temperature field by their complicated interactions with primary vortex cells induced by the swirling effects from inner wall rotation. For example, when $\sigma = 0.05$, a four-pairs based Taylor vortex structure, rather than five-pair of vortex cells observed for $\sigma = 0$, arises from the relative weakening effects of the centrifugal forces in the presence of heating. The strength of the Taylor vortex in the positive azimuthal direction θ is seen to be enhanced, while that negative θ direction appear to be diminished and these observations are consistent with the benchmarks results [65,66] and recent numerical simulations [30]. In order to quantify the heat transfer rate in the presence of mixed convection, a mean equivalent thermal conductivity at the inner cylinder can be defined as

$$\overline{k}_{eq}\Big|_i = \frac{lnR_{io}}{\mu}\int_o^H \left(-r\frac{\partial T}{\partial r}\Big|_{r=R_i}\right)dr.$$

Table 4 presents a comparison of the equivalent thermal conductively computed using the axisymmetric cascaded LB formulations against the benchmark results [65,66] for different values of σ. Very good quantitative agrement is seen and this validates the ability of the cascaded LB schemes in the cylindrical coordinate system to represent complex flows with heat transfer.

3.6. Melt flow and convection during Czochralski crystal growth in a rotating cylindrical crucible

As the last test problem, we simulate melt flow and convection during Czochalski crystal growth, based on a configuration reported by Wheeler [67], using our axisymmetric cascaded LB schemes. This Wheeler's benchmark problem involved both forced convection due to the rotation of the crucible and the crystal and natural convection arising from heating effects in the presence of gravity. It has been studied by a variety of numerical schemes (e.g., [68,69,23,31]). The geometric arrangement of this problem is shown in Fig. 13.

Liquid melt in a cylindrical rotating crucible of radius R_c and height H at an angular rotation rate of Ω_c undergoes stirred vortical motion in the meridian plane, which is aided by the angular rotation of the solid crystal of radius R_x at rate Ω_x. In addition, natural convection is set up due to the buoyancy force generated from a differential heating, where the bottom is insulated and its crucible side is maintained at a temperature T_H, while the crystal is at a lower temperature $T_L (i.e., T_L < T_H)$. These can be prescribed in terms of the following boundary conditions, where the (x, z) coordinates are scaled by R_c:

$$\begin{aligned}
&u_r = u_\theta = \tfrac{\partial u_z}{\partial r} = \tfrac{\partial T}{\partial r} = 0 && \text{for } r = 0,\ 0 \leqslant z \leqslant \alpha\\
&u_r = u_z = 0,\ u_\theta = \Omega_c R_c,\ T = T_H && \text{for } r = 1,\ 0 \leqslant z \leqslant \alpha\\
&u_r = u_z = 0,\ u_\theta = r\Omega_c,\ \tfrac{\partial T}{\partial z} = 0 && \text{for } z = 0,\ 0 \leqslant r \leqslant 1\\
&u_r = u_z = 0,\ u_\theta = r\Omega_x,\ T = T_L && \text{for } z = \alpha,\ 0 \leqslant r \leqslant \beta\\
&\tfrac{\partial u_r}{\partial r} = \tfrac{\partial u_\theta}{\partial z} = 0,\ u_z = 0,\ T = T_L + \tfrac{r-\beta}{1-\beta}(T_H - T_L) && \text{for } z = \alpha,\ \beta \leqslant r \leqslant 1
\end{aligned}$$

where $\alpha = H/R_c, \beta = R_x/R_c$. This flow problem is characterized by the following dimensionless parameters: Reynolds numbers due to crucible and crystal rotations $Re_c = R_c^2\Omega_c/\nu$ and $Re_x = R_x^2\Omega_x/\nu$, and Prandtl number $Pr = \nu/\alpha$. We investigate the ability of the axisymmetric cascaded LB schemes for the simulation of mixed convection associated with the Wheeler's benchmark problem for the following two cases: (a) $Re_x = 100, Re_c = -25$ and (b)

Table 4
Comparison of the mean equivalent thermal conductivity at the inner cylinder in a slender vertical cylindrical annulus during mixed convection for $Re = 100, Pr = 0.7$, $R_{io} = 2, \eta = 10$ at different values of σ.

σ	Ref. [66]	Ref. [65]	Present work
0	1.473	1.393	1.395
0.01	1.370	1.383	1.378
0.05	1.324	1.323	1.321

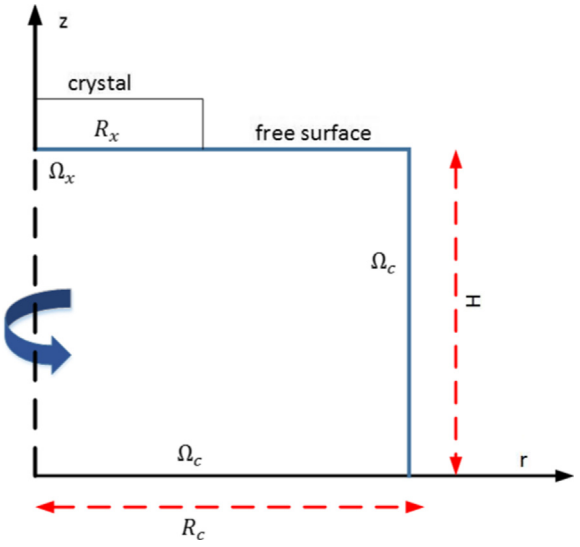

Fig. 13. Geometric arrangement of melt flow and convection during Czochralski crustal growth in a rotating crucible—Wheeler's benchmark problem.

$Re_x = 1000, Re_c = -250$, where the negative sign denotes that the sense of rotation of the crystal is apposite to that of the crucible. We take $Pr = 0.05, \alpha = 1$, and $\beta = 1$ and use a grid resolution of 100×200 for the simulation of both the cases.

Fig. 14 shows the streamlines and isotherm contours in the meridian plane of the liquid melt motion for the two cases. It can be seen that a recirculating vortex appears around the upper left region below the crystal in both cases in addition to the primary vortex. The center of this secondary vortex is found to move to the right at higher Reynolds numbers as a result of higher associated centrifugal forces. On the other hand, the forced convection has modest effect on the temperature distribution, as they are largely alike for both the cases due to the relatively low Reynolds numbers considered.

Table 5 shows the computed absolute maximum values of the streamfunction ψ_{max} for the above two cases and compared with prior numerical results presented in [23,68]. In the pseudo-2D Cartesian coordinates, this is obtained by solving for ψ using $\partial\psi/\partial y = -yu_x$ and $\partial\psi/\partial x = yu_y$. The good agreement confirms that the new axisymmetric cascaded LB schemas presented in this study can effectively simulate complex flow and heat transfer problems in cylindrical geometries.

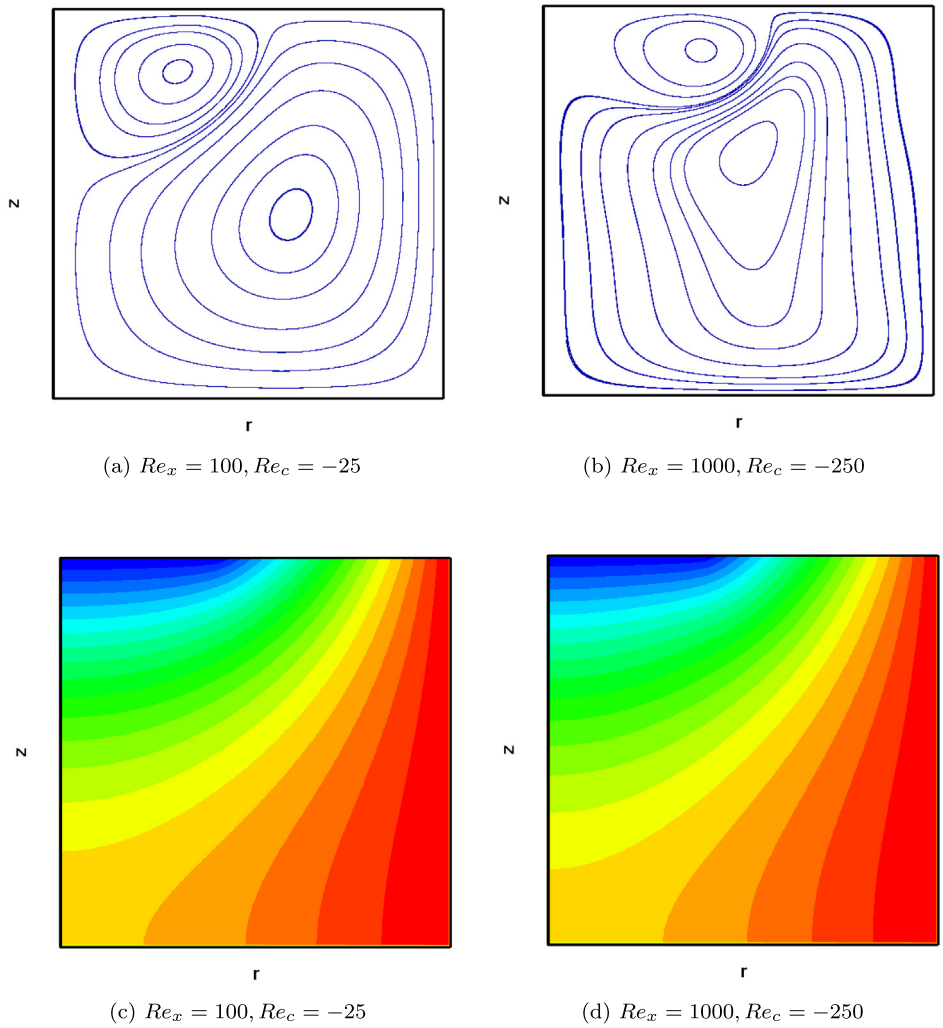

(a) $Re_x = 100, Re_c = -25$ (b) $Re_x = 1000, Re_c = -250$

(c) $Re_x = 100, Re_c = -25$ (d) $Re_x = 1000, Re_c = -250$

Fig. 14. Streamlines (upper row) and isotherms (bottom row) corresponding to two cases of the Wheeler's benchmark problem of melt flow and convection during Czochralshi crystal growth: $Re_x = 100, Re_c = -25$ (left) and $Re_x = 1000, Re_c = -250$ (right).

Table 5
Comparison of the maximum value of the stream function ψ_{max} computed using the axisymmetric cascaded LB schemes with reference numerical solutions for the Wheeler's benchmark problem.

Reference	$Re_x = 10^2, Re_c = -25$	$Re_x = 10^3, Re_c = -250$
Present work	0.1183	1.123
Ref. [70]	0.1140	1.114
Ref. [68]	0.1177	1.148

3.7. Comparison of single relaxation time and cascaded LB models for axisymmetric flow simulations

We will now make a direct comparison between the performance of the single relaxation time (SRT) LB scheme and the proposed cascaded LB formulation based on central moments for axisymmetric flow simulations. In particular, a study of the numerical stability characteristics of these schemes for flow simulations in the cylindrical coordinates represents a key aspect with important practical implications. In this regard, we consider the computation of lid-driven swirling flow in a cylindrical container discussed in Section 3.4, as the flow is set up by a shear in the presence of a geometric singularity between the stationary cylindrical walls and the rotating lid.

For a fixed angular rotation rate Ω of the lid of the cylindrical container of radius R and height H (see Section 3.4 for the nomenclature) at different aspect ratios $R_A = H/A$, we will now make a comparison between the maximum attainable Reynolds number $Re = R^2\Omega/\nu$ with the axisymmetric SRT [22] and cascaded LB schemes. In this regard, we gradually reduce the viscosity, or equivalently, the relaxation time τ for a specific grid resolution until the computation becomes numerically unstable. In the case of the cascaded LB formulation, this is equivalent varying the relaxation times for the second order moments $\omega_j = 1/\tau$, where $j = 4, 5$, and the remaining relaxation times for the higher order moments are set to unity for simplicity.

In particular, for two different grid resolutions of 101×101 and 101×151 corresponding to the aspect ratios R_A of 1.0 and 1.5, respectively, at a fixed angular velocity $\Omega = 0.0014$, simulations are carried out using both these LB models by reducing the relaxation time τ until the computation becomes unstable, which then determines the maximum attainable Re in each case. Since the radius $R = 100$ for both these grid resolution cases, the maximum imposed linear velocity of the cylindrical lid $R\Omega$ is 0.14. The onset of instability is determined when the relative global error increases rapidly as the simulation progress. Such a computational investigation is an extension of those considered for the LB models in the Cartesian coordinates recently [40]. The results are displayed in Fig. 15, which show significant improvements in numerical stability with the use of the axisymmetric cascaded LB approach. It can be seen that the cascaded LB computations can reach Reynolds numbers that are about 7 times higher than those with using the SRT LB scheme for the $R_A = 1.0$, i.e., when the grid resolution used is 100×100. As the cylindrical confined space for the fluid motion undergoing shearing motion becomes narrower and slender ($R_A = 1.5$) that is resolved using 101×150 grid nodes, the maximum attainable Re with the central moments based cascaded LB formulation becomes even higher, by as much as 10 times when compared to the SRT model.

It may be noted that when the cascaded LB scheme is used to solve the governing equations for axisymmetric flows, it incurs about 20% additional computational effort, in terms of the CPU time, when compared to the SRT-LB scheme similar to that observed in the respective 2D Cartesian formulations [40]. On the other hand, the cascaded LB formulation is seen to be much more stable than the SRT scheme. As a result, for practical simulations of axisymmetric flows including swirl effects, the central moments based formulation holds important advantages over other collision models. These significant improvements in numerical stability with cascaded LB schemes, which allow efficient simulation of axisymmetric flows with broader ranges of parameter spaces, for a given resolution is consistent with the recent results obtained for simulations of flows in the Cartesian coordinates [39,40].

4. Summary and conclusions

Thermally stratified fluid convection including rotational effects within cylindrical confined spaces represents an important class of flows with numerous engineering applications. Exploiting axial

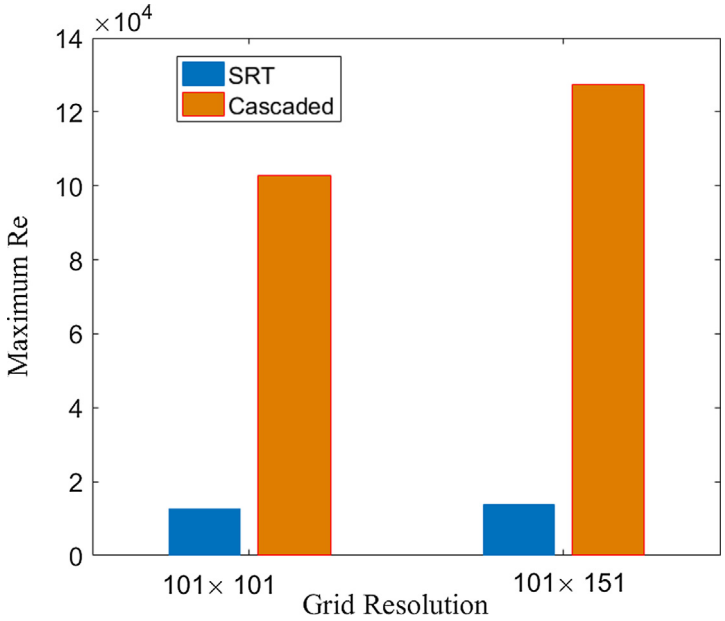

Fig. 15. Comparison of the maximum Reynolds number for numerical stability of single relaxation time (SRT) and cascaded LB methods for simulation of the shear driven swirling flow in a confined cylinder at different grid resolutions.

symmetry in such problems leads to their representation in terms of a quasi-2D system of equations with geometric source terms in the meridian plane, which can significantly reduce computational and memory costs when compared to their full 3D modeling. For example, full 3D solution of the fluid motion and the scalar transport requires typical lattices such as D3Q19 and D3Q7/D3Q15, respectively. On the other hand, axisymmetric LB formulations would require significantly smaller lattice sets resulting in major computational advantages. An important aspect of axial symmetry based models is their suitability to represent reduced 3D problems. In particular, they allow simulations of complex thermal convective flows for broader ranges of parameter spaces (e.g., Rayleigh number/Richardson number/Prandtl number) more efficiently.

In this work, we have presented axisymmetric cascaded LB schemes for convective flows with combined rotation and thermal stratification effects in cylindrical geometries. A triple distribution functions based approach is employed in this regard, in which the axial and radial momentum as well as the pressure field are solved using a D2Q9 lattice based cascaded LB scheme, while the azimuthal momentum and the temperature field are solved using the two other cascaded LB schemes, each based on a D2Q5 lattice. The collision step in these three schemes is based on the relaxation of different central moments at different rates to represent the dynamics of the fluid motion as well as the advection-diffusion transport of the passive scalar fields in a consistent framework. The geometric mass, momentum and energy source terms arising in the quasi-2D formulation are incorporated using a simpler operator splitting based approach involving a symmetric application of their effects given in terms of appropriate change of moments for two half time steps around the collision step. This new computational approach is then used to simulate a variety of complex axisymmetric benchmark thermal flow problems including natural convection between two coaxial cylinders, Rayleigh-Benard convection in a vertical cylinder, mixed convection in a slender vertical annulus between two cylinders under combined rotation and buoyancy forces, and convective flow of a melt during Czochralski crystal growth in a rotating cylindrical crucible. Comparison of the computed results obtained using the axisymmetric cascaded LB schemes for such thermal convective flows for the structures of the flow and thermal fields, as well as the heat transfer rates given in terms of the Nusselt number against prior benchmark numerical solutions demonstrate their good accuracy and validity. Finally, our approach is shown to be second order accurate in grid convergence, and the use of central moments in the cascaded LB formulation leads to significant improvements in numerical stability when compared to other existing LB models for axisymmetric flows.

Conflict of interest statement

The authors wish to confirm that there are no known personal/-financial conflicts of interest with this manuscript.

Acknowledgements

The authors would like to acknowledge the support of the US National Science Foundation (NSF) under Grant CBET-1705630.

Appendix A. Supplementary material

Supplementary data associated with this article can be found, in the online version, at https://doi.org/10.1016/j.ijheatmasstransfer.2018.09.059.

References

[1] H.P. Greenspan, The Theory of Rotating Fluids, Cambridge University Press, London, 1968.
[2] E.L. Koschmieder, Bénard Cells and Taylor Vortices, Cambridge University Press, New York, 1993.
[3] I.V. Shevchuk, Modelling of Convective Heat and Mass Transfer in Rotating Flows, Springer, New York, 2016.
[4] K. Fujimura, Time-dependent vortex breakdown in a cylinder with a rotating lid, Trans. ASME, J. Fluids Eng. 199 (1997) 450–453.
[5] A. Lemembre, J.-P. Petit, Laminar natural convection in a laterally heated and upper cooled vertical cylindrical enclosure, Int. J. Heat Mass Transfer 41 (16) (1998) 2437–2454.
[6] E. Barbosa, O. Daube, A finite difference method for 3d incompressible flows in cylindrical coordinates, Comput. Fluids 34 (8) (2005) 950–971.
[7] A. Guardone, L. Vigevano, Finite element/volume solution to axisymmetric conservation laws, J. Comput. Phys. 224 (2) (2007) 489–518.
[8] X. He, L.-S. Luo, Theory of the lattice Boltzmann method: from the Boltzmann equation to the lattice Boltzmann equation, Phys. Rev. E 56 (6) (1997) 6811.
[9] S. Succi, The Lattice Boltzmann Equation: For Fluid Dynamics and Beyond, Oxford University Press, 2001.
[10] C.K. Aidun, J.R. Clausen, Lattice-Boltzmann method for complex flows, Annu. Rev. Fluid Mech. 42 (2010) 439–472.
[11] T. Krüger, H. Kusumaatmaja, A. Kuzmin, O. Shardt, G. Silva, E.M. Viggen, The Lattice Boltzmann Method, Springer, 2017.
[12] A. Xu, W. Shyy, T. Zhao, Lattice Boltzmann modeling of transport phenomena in fuel cells and flow batteries, Acta Mech. Sinica 33 (3) (2017) 555–574.
[13] L. Mieussens, Discrete-velocity models and numerical schemes for the Boltzmann-BGK equation in plane and axisymmetric geometries, J. Comput. Phys. 162 (2) (2000) 429–466.
[14] I. Halliday, L. Hammond, C. Care, K. Good, A. Stevens, Lattice Boltzmann equation hydrodynamics, Phys. Rev. E 64 (1) (2001) 011208.
[15] K.N. Premnath, J. Abraham, Lattice Boltzmann model for axisymmetric multiphase flows, Phys. Rev. E 71 (5) (2005) 056706.
[16] T. Lee, H. Huang, C. Shu, An axisymmetric incompressible lattice Boltzmann model for pipe flow, Int. J. Mod. Phys. C 17 (05) (2006) 645–661.
[17] T. Reis, T.N. Phillips, Modified lattice Boltzmann model for axisymmetric flows, Phys. Rev. E 75 (5) (2007) 056703.
[18] J.G. Zhou, Axisymmetric lattice Boltzmann method, Phys. Rev. E 78 (3) (2008) 036701.
[19] S. Chen, J. Tölke, S. Geller, M. Krafczyk, Lattice Boltzmann model for incompressible axisymmetric flows, Phys. Rev. E 78 (4) (2008) 046703.
[20] Z. Guo, H. Han, B. Shi, C. Zheng, Theory of the lattice Boltzmann equation: lattice Boltzmann model for axisymmetric flows, Phys. Rev. E 79 (4) (2009) 046708.
[21] H. Huang, X.-Y. Lu, Theoretical and numerical study of axisymmetric lattice Boltzmann models, Phys. Rev. E 80 (1) (2009) 016701.
[22] Q. Li, Y. He, G. Tang, W. Tao, Improved axisymmetric lattice Boltzmann scheme, Phys. Rev. E 81 (5) (2010) 056707.
[23] Y. Peng, C. Shu, Y. Chew, J. Qiu, Numerical investigation of flows in Czochralski crystal growth by an axisymmetric lattice Boltzmann method, J. Comput. Phys. 186 (1) (2003) 295–307.
[24] H. Huang, T. Lee, C. Shu, Hybrid lattice Boltzmann finite-difference simulation of axisymmetric swirling and rotating flows, Int. J. Numer. Methods Fluids 53 (11) (2007) 1707–1726.
[25] S. Chen, J. Tölke, M. Krafczyk, Simulation of buoyancy-driven flows in a vertical cylinder using a simple lattice Boltzmann model, Phys. Rev. E 79 (1) (2009) 016704.
[26] Q. Li, Y. He, G. Tang, W. Tao, Lattice Boltzmann model for axisymmetric thermal flows, Phys. Rev. E 80 (3) (2009) 037702.
[27] L. Zheng, B. Shi, Z. Guo, C. Zheng, Lattice Boltzmann equation for axisymmetric thermal flows, Comput. Fluids 39 (6) (2010) 945–952.
[28] L. Zheng, Z. Guo, B. Shi, C. Zheng, Kinetic theory based lattice Boltzmann equation with viscous dissipation and pressure work for axisymmetric thermal flows, J. Comput. Phys. 229 (16) (2010) 5843–5856.
[29] L. Li, R. Mei, J.F. Klausner, Multiple-relaxation-time lattice Boltzmann model for the axisymmetric convection diffusion equation, Int. J. Heat Mass Transfer 67 (2013) 338–351.
[30] Z. Wang, W. Zhang, J. Zhang, Lattice Boltzmann simulations of axisymmetric natural convection with anisotropic thermal diffusion, Int. J. Heat Mass Transfer 101 (2016) 1304–1315.
[31] Y. Wang, C. Shu, C. Teo, A fractional step axisymmetric lattice Boltzmann flux solver for incompressible swirling and rotating flows, Comput. Fluids 96 (2014) 204–214.
[32] Z. Wang, N. Dang, J. Zhang, A modified lattice Bhatnagar-Gross-Krook model for axisymmetric thermal flow, Int. J. Heat Mass Transfer 108 (2017) 691–702.
[33] Y. Qian, D. d'Humières, P. Lallemand, Lattice BGK models for Navier-Stokes equation, EPL (Europhys. Lett.) 17 (6) (1992) 479.
[34] D. d'Humières, I. Ginzburg, M. Krafczyk, P. Lallemand, L.-S. Luo, Multiple–relaxation–time lattice Boltzmann models in three dimensions, Philos. Trans. Roy. Soc. Lond. A 360 (1792) (2002) 437–451.
[35] M. Geier, A. Greiner, J.G. Korvink, Cascaded digital lattice Boltzmann automata for high Reynolds number flow, Phys. Rev. E 73 (6) (2006) 066705.
[36] P. Asinari, Generalized local equilibrium in the cascaded lattice Boltzmann method, Phys. Rev. E 78 (1) (2008) 016701.

[37] K.N. Premnath, S. Banerjee, Incorporating forcing terms in cascaded lattice Boltzmann approach by method of central moments, Phys. Rev. E 80 (3) (2009) 036702.
[38] K.N. Premnath, S. Banerjee, on the three dimensional central moment lattice-Boltzmann method, J. Stat. Phys. 43 (2011) 747–749.
[39] M. Geier, M. Schönherr, A. Pasquali, M. Krafczyk, The cumulant lattice Boltzmann equation in three dimensions: theory and validation, Comput. Math. Appl. 70 (4) (2015) 507–547.
[40] Y. Ning, K.N. Premnath, D.V. Patil, Numerical study of the properties of the central moment lattice Boltzmann method, Int. J. Numer. Meth. Fluids 82 (2016) 59–90.
[41] A. De Rosis, Non-orthogonal central moments relaxing to a discrete equilibrium: a D2Q9 lattice Boltzmann model, EPL (Europhys. Lett.) 116 (4) (2017) 44003.
[42] F. Hajabdollahi, K.N. Premnath, Improving the low mach number steady state convergence of the cascaded lattice Boltzmann method by preconditioning, Comput. Math. Appl. https://doi.org/10.1016/j.camwa.2016.12.034.
[43] F. Hajabdollahi, K.N. Premnath, Galilean-invariant preconditioned central-moment lattice Boltzmann method without cubic velocity errors for efficient steady flow simulations, Phys. Rev. E 97 (5) (2018) 053303.
[44] K.V. Sharma, R. Straka, F.W. Tavares, New cascaded thermal lattice Boltzmann method for simulations of advection-diffusion and convective heat transfer, Int. J. Therm. Sci. 118 (2017) 259–277.
[45] L. Fei, K.H. Luo, C. Lin, Q. Li, Modeling incompressible thermal flows using a central-moments-based lattice Boltzmann method, Int. J. Heat Mass Transfer 120 (2018) 624–634.
[46] F. Hajabdollahi, K.N. Premnath, Central moments-based cascaded lattice Boltzmann method for thermal convective flows in three-dimensions, Int. J. Heat Mass Transfer 120 (2018) 838–850.
[47] L. Fei, K.H. Luo, Consistent forcing scheme in the cascaded lattice Boltzmann method, Phys. Rev. E 96 (5) (2017) 053307.
[48] L. Fei, K.H. Luo, Q. Li, Three-dimensional cascaded lattice Boltzmann method: Improved implementation and consistent forcing scheme, Phys. Rev. E 97 (5) (2018) 053309.
[49] L. Fei, K.H. Luo, Cascaded lattice Boltzmann method for incompressible thermal flows with heat sources and general thermal boundary conditions, Comput. Fluids 165 (2018) 89–95.
[50] F. Hajabdollahi, K.N. Premnath, Symmetrized operator split schemes for force and source modeling in cascaded lattice Boltzmann methods for flow and scalar transport, Phys. Rev. E 97 (6) (2018) 063303.
[51] P.J. Dellar, An interpretation and derivation of the lattice Boltzmann method using strang splitting, Comput. Math. Appl. 65 (2013) 129–141.
[52] D. Contrino, P. Lallemand, P. Asinari, L. Luo, Lattice-Boltzmann simulations of the thermally driven 2D square cavity at high Rayleigh numbers, J. Comput. Phys. 257 (2014) 257–272.
[53] G. Taylor, Stability of a viscous liquid contained between two rotating cylinders, Philos. Trans. Roy. Soc. Lond. A 223 (1923) 289–343.
[54] H. Yoshida, M. Nagaoka, Multiple-relaxation-time lattice Boltzmann model for the convection and anisotropic diffusion equation, J. Comput. Phys. 229 (20) (2010) 7774–7795.
[55] R. Kumar, M. Kalam, Laminar thermal convection between vertical coaxial isothermal cylinders, Int. J. Heat Mass Transfer 34 (1991) 513.
[56] M. Venkatachalappa, M. Sankar, A. Natarajan, Natural convection in an annulus between two rotating vertical cylinders, Acta Mech. 147 (2001) 173.
[57] S. Liang, A. Vidal, A. Acrivos, Buoyancy-driven convection in cylindrical geometries, J. Fluid Mech. 36 (2) (1969) 239–258.
[58] K. Hourigan, L. Graham, M. Thompson, Spiral streaklines in pre-vortex breakdown regions of axisymmetric swirling flows, Phys. Fluids 7 (12) (1995) 3126–3128.
[59] K. Fujimura, H. Yoshizawa, R. Iwatsu, H.S. Koyama, J.M. Hyun, Velocity measurements of vortex breakdown in an enclosed cylinder, J. Fluids Eng. 123 (3) (2001) 604–611.
[60] A.Y. Gelfgat, P. Bar-Yoseph, A. Solan, Stability of confined swirling flow with and without vortex breakdown, J. Fluid Mech. 311 (1996) 1–36.
[61] E. Serre, P. Bontoux, Vortex breakdown in a three-dimensional swirling flow, J. Fluid Mech. 459 (2002) 347–370.
[62] H.M. Blackburn, J. Lopez, Symmetry breaking of the flow in a cylinder driven by a rotating end wall, Phys. Fluids 12 (11) (2000) 2698–2701.
[63] S. Bhaumik, K. Lakshmisha, Lattice Boltzmann simulation of lid-driven swirling flow in confined cylindrical cavity, Comput. Fluids 36 (7) (2007) 1163–1173.
[64] J. Zhou, Axisymmetric lattice Boltzmann method revised, Phys. Rev. E 84 (2011) 036704.
[65] C.J. Ho, F.J. Tu, An investigation of transient mixed convection of cold water in a tall vertical annulus with a heated rotating inner cylinder, Int. J. Heat Mass Transfer 36 (1993) 2847–2859.
[66] K.S. Ball, B. Farouk, On the development of Taylor vortices in a vertical annulus with a heated rotating inner cylinder, Int. J. Numer. Meth. Fluids 7 (1987) 857–867.
[67] A. Wheeler, Four test problems for the numerical simulation of flow in Czochralski crystal growth, J. Cryst. Growth 102 (4) (1990) 691–695.
[68] D. Xu, C. Shu, B.C. Khoo, Numerical simulation of flows in Czochralski crystal growth by second-order upwind QUICK scheme, J. Cryst. Growth 173 (1997) 123–131.
[69] C. Shu, Y. Chew, Y. Liu, An efficient approach for numerical simulation of flows in Czochralski crystal growth, J. Cryst. Growth 181 (4) (1997) 427–436.
[70] Y. Peng, C. Shu, Y.T. Chew, J. Qiu, Numerical investigation of flows in Czochralski crystal growth by an axisymmetric lattice Boltzmann method, J. Comput. Phys. 186 (2003) 295–307.